ACS APPLIED ENERGY MATERIALS

www.acsaem.org Article

Kinetic Rejuvenation of Li-Rich Li-Ion Battery Cathodes upon Oxygen Redox

Jinhyuk Lee, Daiwei Yu, Zhi Zhu, Xiahui Yao, Chao Wang, Yanhao Dong, Rahul Malik, and Ju Li*

Cite This: *ACS Appl. Energy Mater.* 2020, 3, 7931−7943 Read Online

ACCESS | Metrics & More | Article Recommendations | Supporting Information

ABSTRACT: Minimizing internal structural rearrangements upon oxygen redox is currently considered the chief guideline for designing high-performance Li-rich cathodes for Li-ion batteries. In contrast, our study of Li-rich layered- and disordered-rocksalt cathodes reveals that while global oxygen mobility promoted upon O-redox can be damaging, disruption of a local structural order [*e.g.*, medium-range-order (MRO)] triggered by O-redox and associated volume expansion are highly beneficial as they reduce the Li-transport resistance in the materials, that is, the Li-rich cathodes become "rejuvenated" by this process. Furthermore, we use this knowledge to inform a molten-salt treatment to predisturb the MRO, expand crystal volume before cycling, and endow a surface gradient composition for highly Li-rich Co-free layered cathodes, such that the treated materials can achieve high capacity (>230 mA h/g) from the very first cycle with excellent rate capability (154 mA h/g at 2 A/g) and outstanding capacity/voltage-retention (∼4% capacity-loss, ∼140 mV voltage-loss after 200 cycles at 100 mA/g; >210 mA h/g). From these results, we explain the mechanism and universality of the rejuvenation process in various charge-ordered oxides and propose guidelines for designing advanced Li-rich cathode materials with combined transition-metal- and oxygen-redox activities.

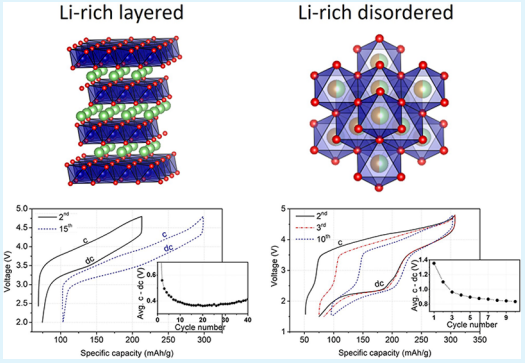

KEYWORDS: *Li-ion battery, Li-rich layered and cation-disordered cathodes, oxygen redox, Li diffusion, rejuvenation, activation, molten-salt treatment*

1. INTRODUCTION

The ever-increasing demand for high-performance, low-cost Li-ion batteries for electric vehicles and grid energy storage calls for high-energy electrodes made with earth-abundant elements. In this regard, Li-rich cathode materials ($x > 1$ in $Li_xTM_{2-x}O_2$, TM = transition metal) with a layered structure (*e.g.*, $Li_{1.2}Ni_{0.13}Mn_{0.54}Co_{0.13}O_2$) or a disordered-rocksalt structure (*e.g.*, $Li_{1.3}Mn_{0.4}Nb_{0.3}O_2$) have received substantial attention as advanced battery cathodes.[1−12] These materials can deliver substantially higher gravimetric capacity (>250 mA h/g) and energy density (>800 W h/kg) compared to traditional materials (*e.g.*, $LiCoO_2$; ∼170 mA h/g, 660 W h/kg). Also, they improve the sustainability of the Li-ion batteries by removing or significantly reducing scarce, expensive, and environmentally unfriendly elements (*e.g.*, Co, Ni) in their structure.[3−12]

In these materials, the theoretical TM-redox capacity is often limited to ∼140 mA h/g because of the limited amount of redox-active TMs in their crystal structure. For instance, for layered $Li^+_{1.2}Ni^{2+}_{0.2}Mn^{4+}_{0.6}O^{2-}_2$, only 0.4 Li, or 126.1 mA h/g, can be extracted in charge through Ni^{2+}/Ni^{4+}-oxidation because Mn^{4+} cations can barely be oxidized to beyond Mn^{4+} in the structure.[8−10] As a result, if one observes higher capacity in the cycling of $Li_{1.2}Ni_{0.2}Mn_{0.6}O_2$, O-redox must additionally take place in the materials, which occurs in local Li-rich environments (*e.g.*, OLi_4TM_2, OLi_5TM_1) around oxygen where there are non-bonding O 2p orbitals (*i.e.*, Li−O−Li states).[13,14] In Li-rich materials containing multiple TMs, the local electroneutrality demands the TM sites in the OLi_4TM_2 or OLi_5TM_1 unit to be occupied by high-valent TM cations (*e.g.*, Ti^{4+}, Mn^{4+}, Nb^{5+}), instead of low-valent ones (*e.g.*, Ni^{2+}), which often results in medium-range-order [MRO, detectable with X-ray diffraction (XRD)] of cations in the Li-rich layered cathodes or short-range-order (SRO) in the Li-rich disordered-rocksalt cathodes.[7−10,15−18] For instance, this tendency leads to the rise of the "Li_2MnO_3-like" MRO (Li_2MnO_3-like domain) in the layered Li- and Mn-rich cathodes,[7−10] and because the nonbonding O 2p orbitals are primarily in the Li_2MnO_3-like domains, O-redox also takes place within the domains.

Received: June 5, 2020
Accepted: July 24, 2020
Published: July 24, 2020

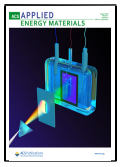

Downloaded via MASSACHUSETTS INST OF TECHNOLOGY on September 16, 2020 at 12:27:01 (UTC).
See https://pubs.acs.org/sharingguidelines for options on how to legitimately share published articles.

© 2020 American Chemical Society

https://dx.doi.org/10.1021/acsaem.0c01315
ACS Appl. Energy Mater. 2020, 3, 7931−7943

Unfortunately, the radical oxygen ion generated upon oxygen oxidation is highly mobile, and as the oxygen is covalently bonded with TMs, this increased O-mobility often accompanies TM migration, triggering reversible or irreversible structural changes in Li-rich materials. This structural changes result in oxygen loss or unwanted phase transformation, which leads to voltage- and capacity-decay.[7−10,19−21] Therefore, minimizing the structural rearrangement while using combined TM- and O-redox has been widely considered as a holy grail to the development of Li-rich cathodes with high capacity and stability.[5,9,19−26] For instance, Bruce *et al.* showed that by changing the superstructure from the "honeycomb" to "ribbon" structure *via* a slight compositional modification, one could suppress the Mn-migration upon O-redox in the layered Na−(Li, Mn)−O cathode to reduce voltage hysteresis.[22] Also, Kang *et al.* recently revealed that by utilizing the O2-type layered structure instead of the O3-type, irreversible cationic migration during O-redox could be mitigated for layered Li-rich and Mn-rich cathodes, leading to improved voltage retention.[26] Besides the layered cathodes, Li-rich disordered-rocksalt cathodes also experience structural damages upon O-oxidation, such as the oxygen loss via cation-densification; hence, its mitigation by various methods (*e.g.*, fluorination) has been at the center of its research.[5,25] Finally, numerous doping (*e.g.*, Ti^{4+}, F^{-}, Cd^{2+}, and S^{2-}) and coating strategies (*e.g.*, coating of AlF_3, $LaPO_4$) were adopted, emphasizing the importance of minimal structural changes in Li-rich materials.[23−30] As such, internal structural evolution upon O-redox has been widely considered as a pathological phenomenon to suppress for Li-rich cathode materials.

In this study, we reveal that, in contrast to the prevailing opinion, the O-redox-assisted structural change can be highly beneficial to the performance of Li-rich cathodes by substantially reducing the internal Li-transport resistance. We synthesized highly Li-rich layered cathodes (nominally $Li^{+}_{1.25}Ni^{2+}_{0.125}Mn^{4+}_{0.625}O^{2-}_{2}$ and $Li^{+}_{1.25}Ni^{3+}_{0.25}Mn^{4+}_{0.50}O^{2-}_{2}$) with minimal Ni and no Co, which possess the Li_2MnO_3-type MRO. Because the small Ni content in the materials limits the theoretical Ni-redox capacity (∼81 mA h/g for both compounds), a high level of O-redox must additionally occur for these materials to achieve a high cycling capacity. The initial capacities of these materials are low; yet, they undergo "rejuvenation" upon extended cycling with substantial improvements in performance (reduced hysteresis and more capacity), which correlates with disruption of the MRO and associated volume expansion initiated by O-redox-facilitating TM migration. Moreover, we show, for the first time, that an essentially similar process occurs for a disordered-rocksalt-type Li-rich cathode ($Li_{1.2}Ni_{1/3}Ti_{1/3}Mo_{2/15}O_2$), suggesting the *universality* of this rejuvenation process.

We use this newfound insight to inform a molten-salt treatment to predisturb the MRO and increase the crystal volume before cycling and to endow a surface gradient composition for improved cycling stability. As a result, the treated materials can deliver outstanding performance from the first cycle, including increased capacity, high power capability, and excellent capacity/voltage retention. In particular, one of the treated-$Li_{1.25}Ni_{0.25}Mn_{0.50}O_2$ delivers 154 mA h/g even at a very high rate of 2 A/g and loses only about 4% of its ∼215 mA h/g-capacity and 140 mV of discharge voltage upon 200 cycles at 100 mA/g. Based on these results, we discuss the mechanism and universality of the rejuvenation process in various charge-ordered Li-rich cathodes and reveal the balancing act between the local-oxygen-mobility and global-oxygen-mobility in the performance of Li-rich cathodes. Our mechanistic insight about the rejuvenation process and demonstration of high-performing Co-free Li-rich cathodes guide us to exciting new directions in the design of advanced cathode materials with combined TM- and O-redox activities.

2. EXPERIMENTAL SECTION

2.1. Material Synthesis. $Li_{1.25}Ni_{0.125}Mn_{0.625}O_2$ (N125) and $Li_{1.25}Ni_{0.25}Mn_{0.50}O_2$ (N250) powders were synthesized from mixed nickel−manganese carbonate precursors ($Ni_{1/6}Mn_{5/6}CO_3$ for N125; $Ni_{1/3}Mn_{2/3}CO_3$ for N250) obtained *via* a coprecipitation method. Using a separating funnel, a 0.2 M mixed $NiSO_4$ (Sigma-Aldrich, ACS, ≥98%) and $MnSO_4$ (Amresco, 98%) aqueous solution (250 mL) (Ni/Mn = 1:5 for N125; and 1:2 for N250) were added drop-wise to an equal volume (250 mL) of a 1 M $NaHCO_3$ (Alfa Aesar, 99.7−100.3%) aqueous solution under constant stirring of 200 rpm at 50 °C. The pH was adjusted to be 8−9 by adding ammonium hydroxide. The mixed solution containing green precipitates that are formed immediately was aged for 12 h under the same conditions of the coprecipitation procedure. The nickel−manganese carbonate precipitate was collected from the solution using a centrifuge, washed with deionized water several times, and dried overnight at 110 °C in a vacuum oven. The dried powder was mixed with 5% excess of the stoichiometric amount of Li_2CO_3 (Alfa Aesar, ACS, 99% min) to compensate for the possible loss of lithium during calcination. The mixture was heated at 500 °C for 3 h in a box furnace in air. Then, after cooling down, the resulting powder was manually mixed using a mortar and a pestle. Finally, the mixture was reheated at 900 °C for 6 h in a box furnace in air to form N125 and N250. $Li_{1.2}Ni_{1/3}Ti_{1/3}Mo_{2/15}O_2$ (a disordered-rocksalt Li-rich cathode, LNTMO) was made with a stoichiometric amount of Li_2CO_3 (Alfa Aesar, ACS, 99% min), $NiCO_3$ (Alfa Aesar, 99%), TiO_2 (Alfa Aesar, 99.9%), and MoO_2 (Alfa Aesar, 99%) as precursors. The precursors were dispersed into acetone and ball-milled for 10 h at 300 rpm and then dried overnight in a vacuum oven. The precursor mixture was heated at 750 °C for 2 h in air to form the desired LNTMO phase.

The molybdate molten-salt treatment was conducted as reported by Zhu *et al.*[21] First, the desired amount (30.66 mg for the "5M" treatment and 61.32 mg for the "10M"-treatment) of ammonium molybdate tetrahydrate (AMT) (Sigma-Aldrich) was dissolved into 5 mL of deionized water. Then, 500 mg of N125 or N250 powders was added into the ammonium molybdate solution. Such a weight ratio between the AMT salt and the N125/N250 powder translates into 5 wt % (25 mg) MoO_3 compared to the N125/N250 powder (500 mg) for the "5M" sample and 10 wt % (50 mg) MoO_3 for the "10M" samples. The pH of the mixed solution was adjusted to ∼10 by adding the ammonium hydroxide solution. The solution was stirred and heated at 600 rpm at 80 °C using a hot stirring plate, during which the water in the solution was evaporated. After the initial drying at the hot plate, the sample was further dried at 110 °C for 5 h in a vacuum oven. After the drying process, the mixed powder was collected from a vial and manually mixed again to more uniformly distribute the AMT salt in the powder mixture. Then, the salt-powder mixture was heated at 800 °C for 5 h in air using a box furnace, during which the AMT salt reacts with the N125 or N250 powder to form Li_2MoO_4 and leach lithium and oxygen from the surface of the N125 or N250 particles. After cooling, Li_2MoO_4 was removed from the 5M- or 10M-treated N250/N125 samples by washing several times with deionized water. Finally, the treated samples were dried in a vacuum oven (110 °C) overnight.

2.2. Electrochemical Measurements. To prepare a cathode film from the (AMT-treated) N250/N125 samples, a slurry of 80 wt % active material, 10 wt % carbon black (TIMCAL, Super C65), and 10 wt % polyvinylidene fluoride binder dissolved in *N*-methyl-1,2-pyrrolidone (NMP, Sigma-Aldrich, 99.5%) was cast onto aluminum foils using a doctor-blade. NMP was evaporated at 110 °C for 4 h in a vacuum oven. Coin cells (CR2032) were assembled with the cathode, the Li-counter electrode, a separator (Celgard 2400), and a 1 M

https://dx.doi.org/10.1021/acsaem.0c01315
ACS Appl. Energy Mater. 2020, 3, 7931−7943

solution of $LiPF_6$ in a mixture of ethyl carbonate/dimethyl carbonate (EC/DMC, 1:1 v/v) in an Ar-filled glove box. The active material's loading on the cathode film was ∼5 mg/cm^2. The galvanostatic charge/discharge, intermittent titration tests, and rate-capability tests were performed using a potentiostat (LAND CT2001, China) at room temperature otherwise specified. The specific capacity was calculated based on the amount of the active material in the cathode film. The electrochemical testing protocol was the same for the LNTMO cathode. However, the LNTMO cathode film was made using a dry method. The LNTMO powder and carbon black (TIMCAL, Super C65) were first manually mixed in the weight ratio of 70:20 using a mortar and pestle. Then, polytetrafluoroehylene (PTFE, DuPont, Teflon 8A) was added to the mixture as a binder, such that the film is made of 70 wt % of the LNTMO powder, 20 wt % of the carbon black, and 10 wt % of the PTFE binder. The components were manually mixed again and rolled into a thin cathode film using a stainless steel rod and a plate inside an Ar-filled glove box.

2.3. Material Characterization. The XRD patterns for the as-prepared compounds and on electrodes were collected on a PANalytical multipurpose diffractometer (Cu source) in the 2θ range of 15−85°. To perform XRD on the cycled electrodes, the coin cells were disassembled in an Ar-filled glovebox and washed with DMC. Then, the electrode film was placed on a glass slide and sealed with Prolene thin film (Chemplex SpectroMembrane 3018) and vacuum grease. The Rietveld refinement on the collected XRD patterns was completed using PANalytical X'pert HighScore Plus software. Scanning electron microscopy (SEM) images were collected on a Zeiss Merlin high-resolution SEM. Elemental analysis of the compounds was performed with inductively coupled plasma−optical emission spectrometry (ICP−OES, Agilent ICP−OES VDV 5100) for lithium, nickel, and manganese. The high-angle annular bright-field (HAABF) images and electron energy loss spectroscopy (EELS) spectra are acquired from a JEOL ARM 200F scanning transmission electron microscope (STEM) operated at 200 keV, equipped with a cold field emission gun and integrated aberration (Cs) corrector. Dual EELS spectrometers are used to collect both the low-loss and high-loss spectra, and the low-loss spectra are utilized to correct the drift of the zero-loss peak (ZLP). Based on the full width at half-maximum of the ZLP, the optimal energy-resolution of EELS is about 1 eV. After ZLP drift correction, EELS quantification was performed by using a signal integration window of 50 eV, the Hartree−Slater model of the partial ionization cross section, and power-law background subtraction. The STEM−EELS sample is prepared using FEI Helios NanoLab 600 DualBeam FIB/SEM equipped with the Ga-ion source. A platinum layer is deposited on top of the cathode particle to protect it before the lift-out. The X-ray photoelectron spectroscopy (XPS) measurement was conducted using a Physical Electronics VersaProbe II X-ray Photoelectron Spectrometer.

3. RESULTS AND DISCUSSION

3.1. Synthesis and Characterization of Highly Li-Rich Co-Free Layered Cathodes. We chose to make $Li^+_{1.25}Ni^{2+}_{0.125}Mn^{4+}_{0.625}O^{2-}_2$ (N125) and $Li^+_{1.25}Ni^{3+}_{0.250}Mn^{4+}_{0.500}O^{2-}_2$ (N250) in our study because of our interest in identifying Co-free Li-rich materials with very low Ni-content. The two materials were synthesized by a solid-state reaction. The elemental analysis *via* ICP−OES show that the actual Li/Ni/Mn ratio is 1.268:0.121:0.611 for N125 (target ratio = 1.25:0.125:0.625) and 1.274:0.241:0.485 for N250 (target ratio = 1.250:0.25:0.5).

XRD measurement of the materials shows typical patterns of layered Li- and Mn-rich materials (Figure 1a). The Rietveld refinement using the $R\bar{3}m$ structure as an input shows that the a (=b) and c-lattice parameters are 2.8492 Å and 14.2319 Å for N125 and 2.8539 Å and 14.2316 Å for N250 (Figure S1). The peaks between 20° and 25° show the presence of $LiMn_6$ or $LiMn_5Ni$ superstructures in the TM layers ($C2/m$ Li_2MnO_3-like MRO).[7−10] Figure 1b shows the SEM images of the N125 and N250 particles. Secondary particles with a diameter of 4−5 μm are observed from both materials; the spherical morphology is better developed for the N250 particles than for the N125 particles. The primary particles have the shape of a hexagonal prism for both materials, while the primary particle size is bigger for N125 (300 nm to 1 μm) than for N250 (200−300 nm). Finally, the XPS measurement reveals a greater contribution of the Ni^{3+} signal (at ∼856 eV) compared to the Ni^{2+} signal (at ∼854.8 eV) in the Ni-XPS spectrum of N250 than that of N125 (Figure 1c).[31] This result indicates that the Ni-oxidation state at the particle surface is higher for N250 (∼2.7+) than for N125 (∼2.36+), as expected based on their composition. The Mn oxidation state is ∼4+ for both materials (Figure S2).

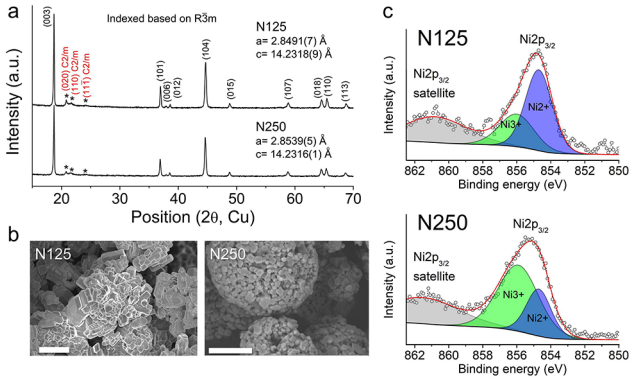

Figure 1. Characterization of two highly-Li-rich layered cathode materials. (a) XRD patterns of $Li_{1.25}Ni_{0.125}Mn_{0.625}O_2$ (N125) and $Li_{1.25}Ni_{0.250}Mn_{0.500}O_2$ (N250), (b) SEM images of N125 and N250. Scale bar: 2 μm. (c) Ni $2p_{3/2}$ peak of N125 and N250 obtained from the XPS.

3.2. Electrochemical Performance of N125 and N250. We performed galvanostatic cycling tests to evaluate their electrochemical behavior (2.0−4.8 V, 20 mA/g, room temperature). Figure 2a,b show the voltage profile of N125 and N250, respectively. During the first charge, N125 and N250 exhibit a sloping curve up to ∼4.5 V, and then, a ∼4.6 V plateau follows, which is typical behavior of Li-rich layered cathodes: the sloping-charge involves TM-oxidation (*e.g.*, Ni-oxidation), and the following plateau comes with O-oxidation in the bulk structure, where some O-loss at the particle surface is an undesirable side effect.[8−10,32,33] The 1st discharge capacity of N125 and N250 is 128 mA h/g and 161 mA h/g, respectively, which is quite low compared to the initial discharge capacity (>230 mA h/g) of standard Li-rich layered cathodes with higher TM-content (*i.e.*, less Li-rich).[7−10] On the other hand, there is a slow increase in their capacity upon cycling, which results in the stable discharge capacity to above 220 mA h/g for N125 and 210 mA h/g for N250. In particular, the capacity remains nearly the same for N250 during its 50th (211.3 mA h/g) to 200th cycles (214.2 mA h/g) (Figure 2c).

Voltage-profile analysis reveals that this increase of capacity accompanies a notable reduction of internal resistance during the initial 20 cycles. Figure 2d,e shows the 2nd and 15th charge/discharge profiles of N125 and N250, respectively. For both cases, voltage hysteresis (*i.e.*, overpotential) is substantially smaller in the 15th cycle compared to the 2nd cycle. Also, during the 2nd to 20th cycles, the difference between the average charging and discharging voltage *decreases* by as much as 200 mV (from 0.56 V to 0.36 V) for N125 and by 160 mV

https://dx.doi.org/10.1021/acsaem.0c01315
ACS Appl. Energy Mater. 2020, 3, 7931−7943

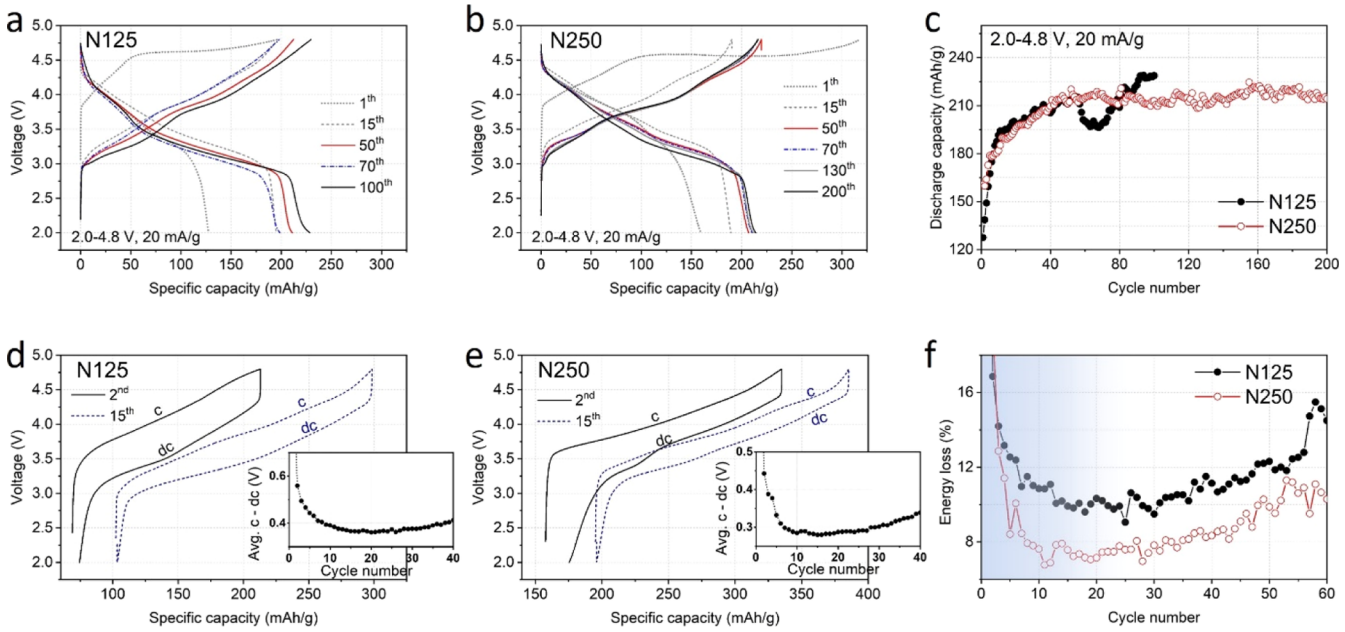

Figure 2. Rejuvenation process in N125 and N250. The voltage profile of (a) N125, and (b) N250, when they are cycled at 20 mA/g at room temperature between 2.0 V and 4.8 V and (c) their discharge capacity. The 2nd and 15th charging and discharging profiles of (d) N125 and (e) N250. The insets show the difference between the average charging- and discharging-voltage of the two materials as a function of the cycle number. (f) Energy loss (%; 100 − 100 × discharge energy/charge energy) of N125 and N250 during the cycling.

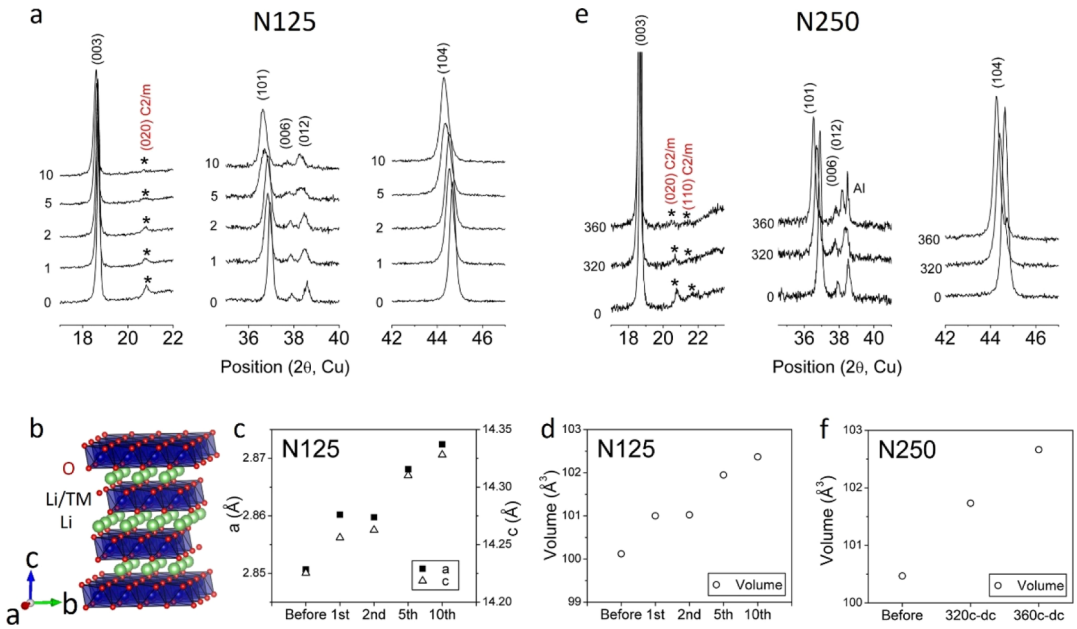

Figure 3. Structure evolution of N125 and N250 cathodes upon cycling. (a) XRD patterns of the N125 cathode before cycling and after the 1st, 2nd, 5th, and 10th cycles (2.0−4.8 V, 20 mA/g). (b) Schematic of the layered lithium-TM oxide structure. The change of the (c) *a*- and *c*-lattice parameters and (d) volume of N125 during the cycling. (e) XRD patterns of the N250 cathode before cycling and after the 1st discharge. Here, one cell was charged to 360 mA h/g, and another was charged to 320 mA h/g before the 1st discharge. (f) Volume of the N250 cathode before and after the first cycle.

(from 0.44 V to 0.28 V) for N250 (the insets in Figure 2d,e). This reduction of voltage hysteresis is intriguing because the hysteresis generally becomes worse upon cycling because of the accumulation of side-reaction products at the cathode/electrolyte interface or by irreversible structural damages during cycling.[8−10,34] This alleviation of voltage hysteresis indicates that Li-cycling kinetics is instead being upgraded or activated: as a result, we observe a drastic decrease in their energy inefficiency during the early cycles (Figure 2f). However, after ∼20 cycles, the polarization and energy inefficiency start increasing slowly for both compounds, suggesting that Li-cycling kinetics becomes degraded after the early improvements. We discuss this in more detail in Section 3.7. Also, we will show later in this paper (Section 3.6) that a virtually identical process (*i.e.*, hysteresis reduction) occurs for a disordered-rocksalt-type Li-rich cathode as well.

3.3. Structural Evolution of N125 and N250 during Cycling. To understand the electrochemical behavior, we

https://dx.doi.org/10.1021/acsaem.0c01315
ACS Appl. Energy Mater. 2020, 3, 7931−7943

studied the structural evolution of the materials upon cycling. Figure 3a shows the XRD patterns of the N125 electrode before cycling and after the 1st, 2nd, 5th, and 10th cycles (2.0−4.8 V, 20 mA/g). The XRD peaks, including (003), (101), (006), (012), and (104) peaks, shift to lower angles, indicating the increase of the lattice parameters of the layered structure. A schematic of the layered structure is shown in Figure 3b. The XRD refinement shows that after the 10 cycles, the *a*-lattice parameter (=*b*-lattice parameter) increases from 2.850(7) Å to 2.872(4) Å, and the *c*-lattice parameter increases from 14.225(3) Å to 14.328(1) Å, which translates into volume expansion from 100.121 $Å^3$ to 102.369 $Å^3$ per unit cell (Figures 3c,d, S3, and Table S1). Moreover, the intensity of the (020)-peak from the $LiMn_6$ or $LiMn_5Ni$ superstructure in the TM layers continues to decrease, indicating the disturbance of the *C*2/*m* MRO. This randomization of in-plane Li/TM ordering has been similarly observed for other Li-rich layered cathodes,[35−37] although the rate at which this phenomenon appears to occur is slower for N125, as evidenced by the *C*2/*m* XRD signal remaining discernible even after the 10th cycle.

N250 exhibits similar behavior. Figure 3e shows the XRD patterns of the N250 electrode before cycling and after the first cycle. In this test, one cell was charged to 320 mA h/g (320-cell), and another cell was charged to 360 mA h/g (360-cell) before discharging. To achieve a 360 mA h/g-charge capacity, the 360-cell was charged at 60 °C instead of room temperature. The XRD peaks shift toward a lower angle after the first discharge, and the shift becomes greater with a higher charging capacity (360 mA h/g). This shift translates into the increase of the N250's volume from 100.469 $Å^3$ (before cycle) to 101.7343 $Å^3$ (320-cell) and 102.664 $Å^3$ (360-cell) per unit cell (Figures 3f, S3, and Table S1). Also, we find a loss of the *C*2/*m* XRD feature; yet, it remains visible after the first discharge. These XRD results, combined with the electrochemical data, suggest that the MRO disruption and associated volume expansion are critical for the Li-rich cathodes to deliver high capacity with reduced internal resistance, that is, such structural changes are beneficial.

Layered Li-rich and Mn-rich cathodes such as $Li_{1.2}Ni_{0.2}Mn_{0.6}O_2$ display a characteristic long and flat charge plateau at 4.5−4.8 V on the first charge, which is often labeled "1st charge Li_2MnO_3 activation" and is associated with Li-extraction from the Li_2MnO_3-like domains in the layered structure with a certain degree of TM migration and O-loss at the particle surface.[8−10] In this sense, we note that the structural changes observed in N125 and N250 are consistent with the "1st charge Li_2MnO_3-activation" description, but in our case, they evolve more incrementally over tens of cycles rather than predominantly in the first cycle. More precisely, we reveal a strong and general relationship between the measured capacity hysteresis and structural evolution. Improved kinetics manifested by reduced hysteresis and increasing capacity correlate with increased MRO disruption and volume expansion upon prolonged cycling. Furthermore, as we will examine in more detail later in the paper, virtually identical structural evolution and reduced voltage hysteresis occur in a disordered-rocksalt Li-rich cathode, which does not possess any "Li_2MnO_3-like" domains, and additionally illustrate that the nomenclature of "1st charge Li_2MnO_3-activation" may be too narrow a description for a more general phenomenon in Li-rich cathodes.

3.4. Thermal Rejuvenation (Pre-activation) of N125 and N250. It is well known in the theory of glasses that a glass retains a memory of its thermal and mechanical history in its atomic structure, in the form of SRO.[38−40] The SRO can evolve at anthropological time scales or beyond, depending on the temperature and mechanical stress at present: if the mechanical stress is zero, the SRO will evolve in the direction of "more ordered" with associated mechanical stiffening and hardening, and this is called aging, whereas under a large enough mechanical stress, there can be plastic strain rate and then the SRO will evolve in the direction of disorder with associated mechanical softening, and this is called "rejuvenation" (as in, going back toward the liquid state where it first came from).[38−40] Such aging or rejuvenation transformation, by definition, is mass-conserving and reversible.

The analogy to our system is the following. Instead of mechanical stress, we have an external voltage driving force from electrochemical cycling (similar to fatigue mechanical loading); instead of structural SRO in the glass, we have MRO in the crystal's chemical order that has a diffraction signature; instead of mechanical softening, we have a reduction of electrochemical kinetic impedance. While the aforementioned rejuvenation at room temperature due to electrochemical cycling is effective, it takes quite a number of cycles to achieve the beneficial effect of the disruption of MRO. Increasing the temperature to above the MRO thermodynamic stability temperature (similar to T_{melt} in glasses), and then quenching down, would be an alternative approach to disrupt the MRO and freeze in this rejuvenated state for the better kinetic performance of Li-rich layered cathodes right from the beginning of room-temperature cycling.

Based on this understanding, we embarked on the thermal acceleration of MRO disruption (pre-rejuvenation) to improve the rate performance of N125 and N250. Because structural rearrangement in Li-rich cathodes often incurs a certain amount of irreversible Li- and O-loss upon cycling,[8−10,32−35] we applied the high-temperature molybdate-molten-salt treatment that can extract Li and O from the cathode particles pre-emptively.[21] We originally pioneered this method to target surface reconstruction of cathode particles to mitigate O-loss. However, for the first time, we will demonstrate below that this method can also be used to thermally disturb the MRO to prerejuvenate the Li-rich materials in the interior, leading to enhanced bulk Li-transport properties. In this treatment, the AMT-salt mixed with the Li-rich cathode particles decomposes into MoO_3 upon heating. Then, MoO_3 reacts with the cathode particles at a high temperature (800 °C) to form Li_2MoO_4, during which there is Li- and O-extraction from the cathode particles: Li_2MoO_4 is later washed away. A detailed procedure is available in Experimental Section (also see Figure S4). One critical advantage of this method over other Li/O-leaching methods (*e.g.*, acid-treatment) is that the degree of leaching can be controlled easily by changing the amount of the AMT salt to that of the active materials.[21,41,42] Also, this treatment can introduce a concentration-gradient-type Li-rich structure: the particle surface is "Li-poor" (*e.g.*, $Li_{0.8}TM_{1.2}O_2$), and the bulk remains "Li-rich" (*e.g.*, $Li_{1.2}TM_{0.8}O_2$).[21] Such a continuous gradient structure is resistant to oxygen loss in subsequent room-temperature electrochemical cycling, like after an "immunization" treatment. In this study, we chose two different salt amounts, such that the total amount of MoO_3 generated upon AMT decomposition would correspond to 5 and 10 wt % of the active material.

https://dx.doi.org/10.1021/acsaem.0c01315
ACS Appl. Energy Mater. 2020, 3, 7931−7943

The XRD patterns of the pristine (N250), 5 wt % MoO_3-treated (5M-N250), and 10 wt % MoO_3-treated (10M-N250) N250-power samples show that the treatment does not change the overall shape of the pattern, indicating that the layered structure is well maintained (Figure 4). However, as the strength of the treatment increases, the XRD peaks [*e.g.*, (104)-peak in the middle inset] systematically shift to lower angles, and the intensity from the superstructure (the left inset) decreases, which indicates that the lattice parameter (volume) of N250 is increasing (the right inset) and the MRO becomes partly disturbed by the treatment (Figure S5). These two changes in the XRD pattern are virtually identical to the changes observed upon electrochemical cycling (Figure 3), which implies that the AMT-treatment has the prerejuvenation effect on the structure of N250. In Supporting Information, we show that N125 shows similar changes in its XRD pattern after the treatment (Figure S6). Note that prerejuvenation by up to the 10M-treatment does not fully disrupt the MRO in the Li-rich crystals, which is most likely because our treatment was performed on lithiated Li-rich layered materials with insufficient cation vacancies that kinetically promote the cation-rearrangement required for full MRO disruption. However, as we will show later, the partial-MRO disruption by the treatment facilitates further electrochemical rejuvenation, overall accelerating the full MRO disruption necessary to achieve high cycling performance.

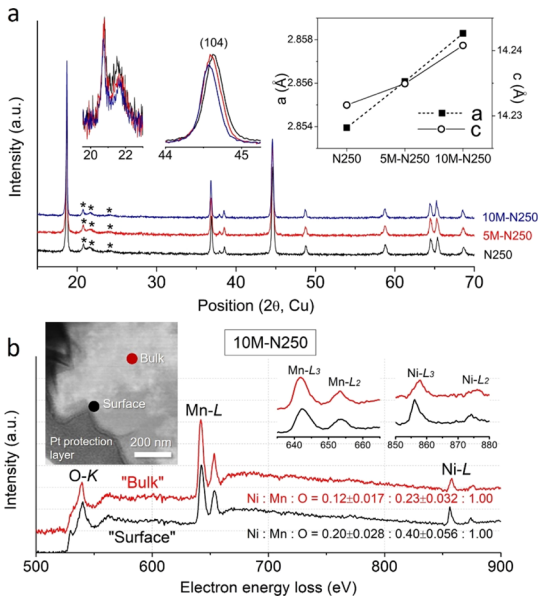

Figure 4. Thermal rejuvenation of the N250 cathode by a molten-salt treatment. (a) XRD patterns of the N250, 5M-N250, and 10M-N250 cathodes. The asterisks (*) show the signal from the $C2/m$ Li_2MnO_3-like domain. The left and middle insets compare the (020) and (110) $C2/m$ superstructure peaks and the (104) $R\bar{3}m$ peak of the three samples, respectively. The right inset shows the *a*- and *c*-lattice parameters of the three samples. (b) EELS data collected from the surface and bulk of a 10M-N250 particle, showing the O-K, Mn-L, and Ni-L edges. The inset HAABF image shows where the data were collected. The two right insets highlight the Mn-L_3 and L_2-edges and Ni-L_3 and L_2 edges in the EELS data.

The EELS data collected from the surface and bulk of a 10M-N250 particle show that this treatment also generates a gradient structure, in which the surface of the cathode particle is "Li-poor" (TM-rich), whereas the bulk remains "Li-rich" (Figure 4b).[21] For this measurement, a thin-sliced 10M-N250 particle sample was prepared with the focused-ion beam (the inset in Figures 4b and S7). The detailed procedure of the EELS measurement can be found in Experimental Section. Relative quantification of the bulk and surface EELS spectra suggests that the atomic ratio between Ni, Mn, and O is 0.12 ± 0.017:0.23 ± 0.032:1 in the bulk and 0.20 ± 0.028:0.40 ± 0.056:1 at the surface, indicating that the particle core is Li-rich (~$Li_xTM_{0.7}O_2$), while the surface is Li-poor (TM-rich; ~$Li_xTM_{1.2}O_2$). Also, this continuous gradient structure for 10M-N250 results in more reduced Ni- and Mn-oxidation states at the particle surface, which is evidenced by that the Ni L_3- and L_2-peaks from the surface are ~1.8 eV lower in energy compared to those from the bulk (the right inset, Figure 4b) and that the Mn L_3/L_2 peak area-ratio is higher at the particle surface (~1.84) compared to that at the bulk (~1.72) (the middle inset, Figure 4b). These XRD and EELS results suggest that the AMT treatment can partially predisturb the MRO in the particle core while endowing a surface gradient composition profile, although additional structural analysis (such as *via* pair distribution function technique) would be needed to further confirm our claim. We would like to emphasize that this is the first report of the thermal MRO-disruption effect (pre-activation) of the AMT treatment, while the surface reconstruction effect was previously examined.[21]

3.5. Electrochemical Performance of Prerejuvenated N250. There is a notable improvement in the performance of N250 after the high-temperature molten-salt treatment. Figure 5a compares the first-cycle voltage profile of N250 (blue), 5M-N250 (red), and 10M-N250 (black) when they are cycled between 2.0 V and 4.8 V at 20 mA/g. We observe a significant increase in the first-discharge capacity and energy density from 161 mA h/g (577 W h/kg) to 196 mA h/g (722 W h/kg) and 235 mA h/g (860 W h/kg) after the 5M- and 10M-treatment, respectively. The voltage profiles of 5M- and 10M-N250 to 70 cycles are shown in Figure 5b,c. Moreover, the number of cycles needed to reach the maximum discharge-capacity and the minimum voltage hysteresis decreases to 5 and 3 cycles for 5M-N250 and 10M-N250, respectively, whereas it takes more than 30 cycles for N250 (Figure S8). At the same time, unlike N250 whose $C2/m$-MRO XRD-feature remains visible after the first cycle, the XRD-feature of 10M-N250 completely disappears after the first cycle (Figure S9), which indicates that "thermal" rejuvenation (partial-MRO-disruption) by the AMT treatment facilitates further "electrochemical" rejuvenation, overall accelerating the "full MRO-disruption" required to achieve high cycling performance.

The GITT test suggests that the capacity increase originates mainly from the improved Li transport. In this test, all materials were equally charged to 320 mA h/g and discharged to 1.5 V at 20 mA/g, with a 5 h relaxation step after every 20 mA h/g charge or discharge step. Figure 5d shows the 1st-discharge GITT profile of N250 (blue), 5M-N250 (red), and 10M-N250 (black), shown as a function of time. Voltage relaxation after each discharge step becomes substantially smaller as the strength of the molten-salt treatment increases. The relaxation in the profile consists of two parts: (i) instant relaxation, which is related to the charge-transfer (CT) resistance at the electrode/electrolyte interface and *IR* drop and (ii) the time-dependent relaxation associated with MT resistance (*i.e.*, Li^+ and polaron diffusion inside the Li-rich oxide).[43,44] The inset in Figure 5d shows an example from 5M-N250. Figure 5e,f shows the contribution of each type in the

https://dx.doi.org/10.1021/acsaem.0c01315
ACS Appl. Energy Mater. 2020, 3, 7931−7943

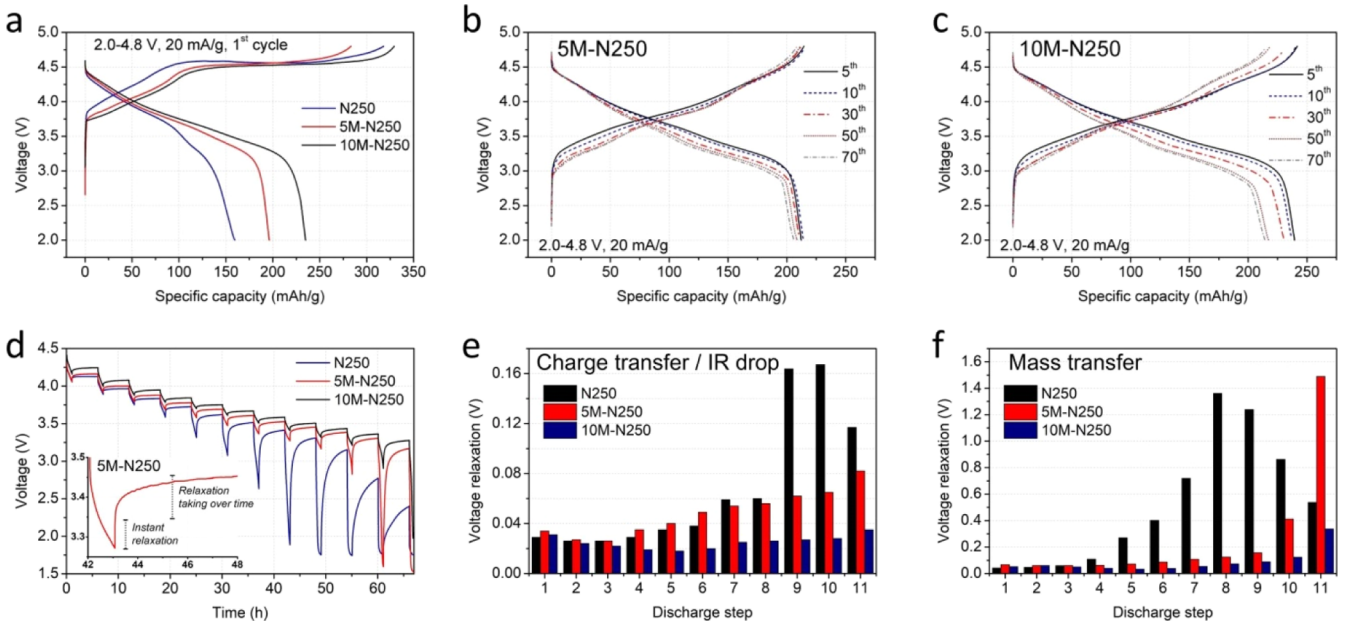

Figure 5. Improvement of the performance of the N250 cathode by the molten-salt treatment. (a) The 1st-cycle voltage profile of the N250, 5M-N250, and 10M-N250 cathodes when cycled between 2 V and 4.8 V at 20 mA/g. The 5th, 10th, 30th, 50th, and 70th cycle voltage profiles of (b) 5M-N250 and (c) 10M-N250 cathodes. (d) Discharge profile during the galvanostatic intermittent titration technique (GITT) test of the N250, 5M-, and 10M-N250 cathodes as a function of time. The inset shows a portion of the 5M-N250 GITT profile, demonstrating the existence of the voltage relaxation that instantly occurs after the current is off and that occurs slowly over time. The former portion is due to the charge-transfer resistance at the cathode/electrolyte interface, and other *IR* drops in the cell. The latter part is related to mass-transfer (MT) resistance. The voltage relaxation upon the GITT discharge of N250, 5M-, and 10M-N250 cathodes, coming from (e) charge-transfer resistance & *IR* drop and from (f) MT resistance.

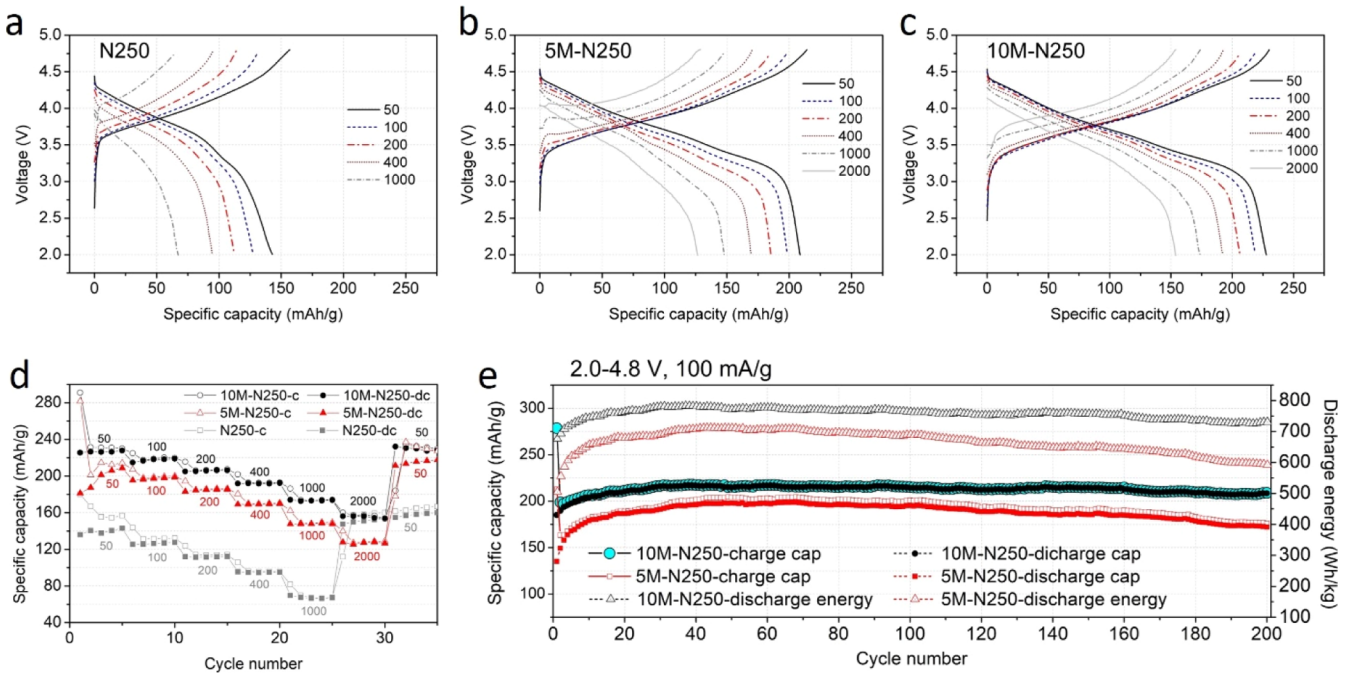

Figure 6. Improved Li-transport after thermal prerejuvenation *via* a high-temperature molten-salt treatment. The representative voltage-profiles of (a) N250, (b) 5M-N250, and (c) 10M-N250 cathodes when they are cycled at different rates; from 50 to 1000 mA/g for N250 and from 50 to 2000 mA/g for 5M- and 10M-N250. (d) Charging and discharging capacities of the three samples during the rate-capability tests. (e) Capacity retention of the 5M- and 10M-N250 cathodes and their discharge energies upon cycling between 2 V and 4.8 V at 100 mA/g for 200 cycles.

GITT curve. The alleviation of voltage relaxation by the molten-salt treatment is substantially greater from the MT source than from the CT/*IR* source. For instance, after the 8th, 9th, and 10th discharge steps (160, 180, and 200 mA h/g-discharge), there is as much as 1.3, 1.15, and 0.75 V-mitigation in the MT polarization by the 10M-treatment, respectively, whereas there is only 0.03, 0.14, and 0.14 V-mitigation for CT/*IR*-drop-polarization. This result suggests that the increased

https://dx.doi.org/10.1021/acsaem.0c01315
ACS Appl. Energy Mater. 2020, 3, 7931−7943

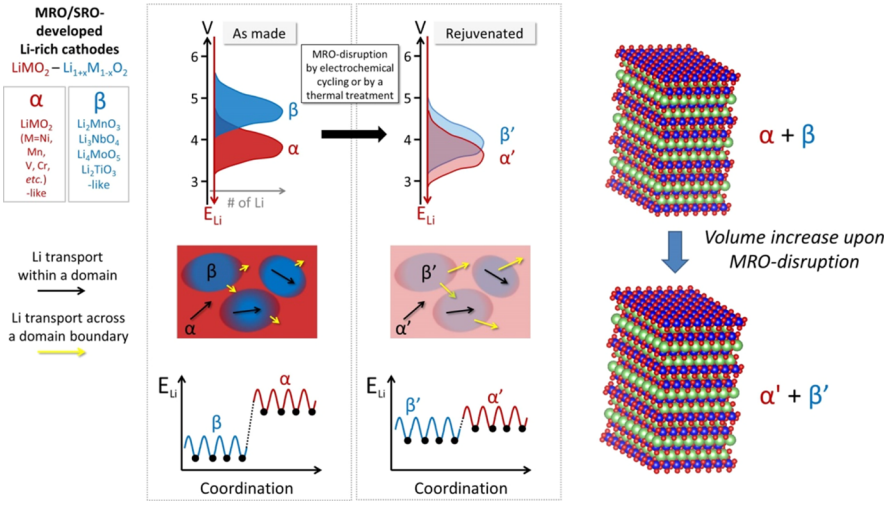

Figure 7. Proposed mechanism of the rejuvenation process in Li-rich cathode materials. The disruption of the MRO (*i.e.*, different domains) in Li-rich materials by electrochemical cycling or by a thermal pretreatment results in a more uniform energy landscape for Li in the Li-rich cathode structure, reducing the energy penalty upon Li transport across different domains. Also, the disruption process increases the volume of the crystal structure, which can facilitate Li transport by providing more space upon Li diffusion.

discharge capacity after the molten-salt treatment is primarily due to the upgraded MT process (bulk Li diffusion) *inside* the cathode structure while the improvement in the CT kinetics (possibly due to surface-carbonate removal or formation of trace molybdenum oxides) should also be beneficial.

This improved kinetics also leads to substantially faster rate performance. Figure 6a–c shows the voltage profiles of N250, 5M-, and 10M-N250 when they are cycled between 2.0 V and 4.8 V at various rates. N250 was subjected to this test without going through the electrochemical rejuvenation. N250 shows a capacity of ∼140 mA h/g when cycled at 50 mA/g, and its capacity decreases to ∼70 mA h/g as the rate increases to 1000 mA/g; 5M-N250 and 10M-N250, on the other hand, deliver ∼125 mA h/g (5M-N250) and ∼150 mA h/g (10M-N250) even at a very high rate of 2000 mA/g. The capacities obtained during the tests are shown in Figure 6d. The 154 mA h/g-capacity at the 2000 mA/g is quite impressive, considering that the capacity of Co-free Li-rich cathodes (*e.g.*, $Li_{1.2}Ni_{0.2}Mn_{0.6}O_2$) typically falls to below 150 mA h/g when the rate increases to above 400 mA/g.[9,45,46] Moreover, the capacity retention of both 5M- and 10M-N250 is also quite exciting (Figure 6e). After 200 cycles at 100 mA/g, the capacity loss of 5M-N250 and 10M-N250 is only 13.5 and 4.0%, respectively, compared to their maximum capacity reached upon cycling (199 mA h/g for 5M-N250; 217 mA h/g for 10M-N250). In Supporting Information, we show that the molten-salt treatment leads to a similar improvement to the performance of the N125 cathode (Figure S10).

3.6. Mechanism and Universality of the Rejuvenation Process. In this study, we highlighted the rejuvenation process in the Li-rich layered cathodes, which reduces the Li-transport resistance in the Li-rich crystal. Also, we demonstrated that high-temperature Li- and O-leaching through the molten-salt treatment could thermally prerejuvenate the Li-rich cathodes. We now provide a more detailed and nuanced explanation for these observations. For the Li-rich layered structure, there are at least two chemical order parameters to consider. One is related to the degree of Li/TM-mixing (cation mixing) "between the Li- and TM-layers," that is, *inter-layer order parameter* ($O_{Inter\text{-}layer}$).[42] The other is about the Li/TM-distribution "within the TM-layers," that is, *intra-layer order parameter* ($O_{Intra\text{-}layer}$). In the Li-rich layered materials, excess Li^+ ions sitting in a TM layer prefer to be surrounded by high-valent TM cations (*e.g.*, Mn^{4+}) to satisfy the local charge neutrality. This preference, in turn, leads to the appearance of the in-plane "$LiMn_6$ or $LiNiMn_5$" honeycomb ordering within the TM layer, instead of random cation distribution.[43] Periodic stacking of the in-plane-ordered TM layers can result in a superstructure, as in $C2/m$-Li_2MnO_3. In typical Li- and Mn-rich layered cathodes that have intermediate compositions between $LiMO_2$ (M = Ni/Mn/Co) and Li_2MnO_3, the development of a "completely" in-plane ordered structure does not happen. Instead, seamlessly integrated "$LiMO_2$-like" and "Li_2MnO_3-like" domains (MRO) evolve within the layered structure.[8−10]

We see the rejuvenation process as a chemical-disordering process triggered by the O-redox-facilitated TM-migration, which increases the randomness of the TM/Li distribution (decreases the order parameters) in the Li-rich compounds. Indeed, the XRD refinement of the N125 electrode suggests that the occupancy of TM cations in the Li layers increases from ∼5 to ∼10% after the first five cycles, indicating the decrease of the $O_{Inter\text{-}layer}$ (Table S1). For now, we are unclear about the reduction of the $O_{Intra\text{-}layer}$ within the TM layers. However, we think it is possible considering that the formation of Li vacancies in the TM layers upon charging can modify the local electrostatic interaction and allow Ni and Mn to rearrange within the TM layer using the Li vacancies. In both cases, the internal order parameter decreases, as evidenced by the disappearance of the in-plane-ordering XRD signal ($C2/m$ MRO-disruption) upon cycling (Figure 3a,e), signifying a decrease of the aforementioned charge-ordering.

Two mechanisms related to the local disorder could facilitate Li transport. First, such a randomization process will make Li-site energies (E_{Li}) within different domains more similar to each other, which reduces the energy penalty when Li^+ ions travel across domain boundaries: Li-site energies (E_{Li}) are higher in the $Li_{1-x}MO_2$-like domains (α/α' = before/after rejuvenation, Figure 7) than in the $Li_{2-x}MnO_3$-like domains

https://dx.doi.org/10.1021/acsaem.0c01315
ACS Appl. Energy Mater. 2020, 3, 7931−7943

(β/β' in Figure 7), as reflected in the lower voltage required to extract Li from the $LiMO_2$-domain (3.5−4.4 V) than from the Li_2MnO_3-like domain (4.5−4.8 V) upon first charging Li- and Mn-rich layered cathodes (Figure 7).[8−10] Such E_{Li}-landscape in the Li-rich structure can slow down Li diffusion by imposing energy-barrier, for example, whenever Li in "low E_{Li}" β-domains needs to travel across "high E_{Li}" α-domains during cycling. Chemical disordering in the $C2m$-Li_2MnO_3 domain is a voltage-lowering process, and this is supported by the well-known voltage-decay issue of Li- and Mn-rich layered cathodes upon the so-called "Li_2MnO_3-activation".[8−10] Because voltage is inversely proportional to E_{Li} in the cathode [$V_{LIB} \propto -(\mu_{Li}^{cathode} - \mu_{Li}^{anode}) \propto -(E_{Li}^{cathode} - E_{Li}^{anode})$; μ = chemical potential],[47] such a decrease of voltage indicates increased E_{Li} within the disrupted $Li_{2-x}MnO_3$-domain (β'). This effectively reduces the E_{Li}-difference between the two domains, hence the domain-boundary energy barrier (Figure 7). Note that the scenario we just described applies to even when the $C2m$-Li_2MnO_3-MRO disruption occurs without any TM exchange between different domains (*e.g.*, local Mn/Li-disorder within the Li_2MnO_3-domain). Such flattening of the E_{Li}-landscape would become even greater if MRO disruption also accompanies interdomain ($\alpha \Leftrightarrow \beta$) TM exchange, as it will move the whole Li-rich crystal toward a solid-solution system without sharp domain boundaries. Also, note that over this entire process, a certain degree of voltage drop would be necessary to adjust the Li-site energies in different domains (hence the boundary energy barrier), although this voltage loss could be minimized if we can engineer the domains to have similar Li-site energies upon material synthesis.

Another possible benefit of MRO disruption for Li transport is the accompanied volume expansion of the Li-rich crystal, which leads to more free volume upon Li diffusion. The MRO-disrupted structure of N125/N250 should be thermodynamically less stable compared to their initial "nanocomposite" structure that formed as a result of being most stable upon synthesis. At a given composition, a crystal with metastable ionic-configuration tends to be larger in volume than that of a stable configuration, that is, larger "free volume" in the analogy of glasses. For instance, theoretical data in the Materials Project show that metastable polymorphs of $LiCoO_2$, such as "*Imma*" (34.649 Å^3), "$C2/m$" (34.744 Å^3) and "$Fd\bar{3}m$" (35.993 Å^3) $LiCoO_2$, have a bigger crystal volume per formula unit than the stable $R\bar{3}m$ $LiCoO_2$ (32.956 Å^3).[48] This metastability-volume correlation can explain why the lattice parameters and volume of N125 or N250 systematically increase upon MRO disruption (Figure 3). Meanwhile, we note that reduced Mn species (Mn^{3+} with a larger ionic radius than Mn^{4+}) created after O loss at the particle surface may further increase the volume of N125 and N250 upon cycling.[8−10] Such increased volume can promote Li transport in the cathode structure for its larger space for relaxation upon Li diffusion (Figure 7).[49,50] For example, it was predicted that even as little as ∼2% volume expansion can decrease the octahedral-tetrahedral-octahedral Li-migration barrier [$E_{migration}$; $D_{Li} \propto \exp(-E_{migration}/k_BT)$] in a rocksalt-type oxide by nearly 40 meV, which corresponds to a five-fold increase of Li-diffusivity at room temperature.[50] Combined with the alleviation of the domain-boundary energy barrier, the expanded volume after MRO disruption can further improve Li transport in N125/N250 (Figures 2 and 3). In this context, one can imagine that the rejuvenation (activation) process can *universally* occur for Li-rich cathodes (not just the so-called Li_2MnO_3-activation in Li/Mn-rich layered cathodes), in which a structure with medium/short-range charge-order develops upon synthesis [$LiMO_2$ (α)−Li_2MnO_3, Li_2TiO_3, Li_3NbO_4, Li_4MoO_5 (β) in Figure 7]; yet, electrochemical cycling partially or fully dissolves the local charge order and increases the free volume.[6,11,16,17,51]

Indeed, we observe a nearly identical process in another Li-rich cathode but now with a disordered-rocksalt structure, $Li_{1.2}Ni_{1/3}Ti_{1/3}Mo_{2/15}O_2$ (LNTMO).[25,44] This material is also known to utilize a large degree of O-oxidation after a limited amount of Ni^{2+}/Ni^{3+}-oxidation in charge.[25,44] Figure 8a,b

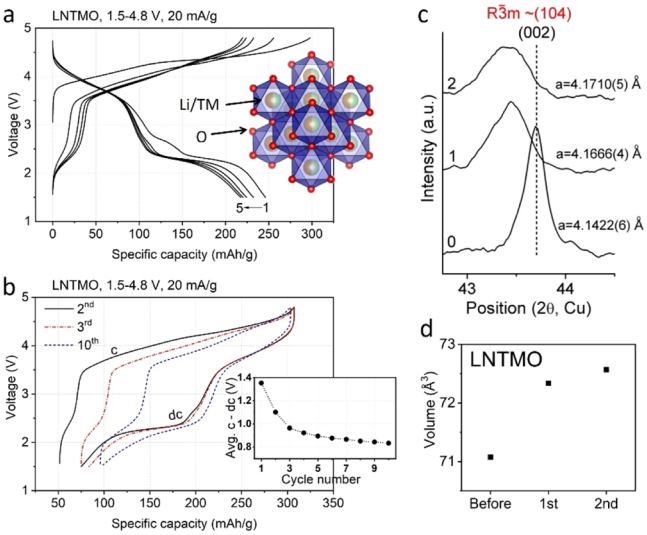

Figure 8. Rejuvenation process in a disordered-rocksalt-type Li-rich cathode. (a) Voltage profiles of the disordered-rocksalt $Li_{1.2}Ni_{1/3}Ti_{1/3}Mo_{2/15}O_2$ (LNTMO) when it is cycled between 1.5 V and 4.8 V at 20 mA/g and room temperature. The inset shows the schematic of the crystal structure. (b) 2nd, 3rd, and 10th charging and discharging profiles of LNTMO: The inset shows the difference between the average charging- and discharging-voltage as a function of the cycle number. (c) $Fm\bar{3}m$ (002) XRD peak of LNTMO before cycling and after 1 and 2 cycles between 1.5 and 4.8 V at 20 mA/g and (d) derived volume.

shows the voltage profiles of LNTMO (1.5−4.8 V, 20 mA/g). As seen from the N125 and N250 (Figure 2d,e), there is significant mitigation of the voltage hysteresis (internal resistance) upon initial cycles, as evidenced by ∼500 mV reduction in the average charge/discharge voltage difference after 10 cycles (Figure 8b). Also, we observe irreversible shifts of the LNTMO's $Fm\bar{3}m$ (002)-XRD peak to a lower angle after initial cycles, confirming that its improved kinetics correlates with the volume expansion as was the case for N125 and N250 (Figure 8c,d). Although further investigation would be needed, we speculate that there is a disruption of the Li_2TiO_3-like SRO (not detectible in XRD) upon O-redox, which was predicted to exist in disordered-rocksalt-type Li-rich Ni^{2+}−Ti^{4+} oxide cathodes.[17] That being said, we realize that quantitative analysis of MRO and SRO in various Li-rich crystals by local-bonding-analyzable characterization tools and computational modeling will play a critical role in understanding the detailed correlation between the degree/type/composition of local chemical order and Li-transport kinetics in the Li-rich materials.[11,18] The analogy of both layered- and disordered-rocksalt Li-rich cathodes to glass aging/rejuvenation under temperature/mechanical stress field (electrochemical cycling here) is indeed quite apt. The fundamental

https://dx.doi.org/10.1021/acsaem.0c01315
ACS Appl. Energy Mater. 2020, 3, 7931−7943

reason is that reversible oxygen redox can reduce the oxygen-migration potential-energy barriers (from 2.3−4.0 eV of O^{2-} to 0.9 eV of O^{-} in the case of $Li_{2-x}MnO_3$ according to Lee and Persson),[52] so that local-oxygen-mobility (LOM) is possible at room temperature, with associated local transition-metal migrations (LMMs) as well, as the TM and oxygen are covalently bonded.[53−55] The LOM-enabled LMM drives the structural rejuvenation of Li-rich cathodes at room temperature with electrochemical cycling. Contrary to popular beliefs, this is intrinsically beneficial. However, what we have not discussed so far is another side to the story, which is global-oxygen-mobiliy (GOM), as a potentially harmful side effect of LOM, if not sufficiently mitigated.[21] While LOM (and the kinetics of aging/rejuvenation in general) can be reversible, GOM is irreversible because the escaped oxygen would react with the electrolyte and also leaves permanent mass deficiency or even dramatic phase changes within the Li-rich cathode crystal.

3.7. Balancing Act between the LOM and GOM. Our understandings provide new directions for the design of high-performance Li-rich cathodes. Poor 1st-cycle Coulombic efficiency (=1st discharge capacity/1st charge capacity) is one of the most critical shortcomings of Li-rich cathodes.[8−10] To achieve high 1st-cycle Coulombic efficiency, the MRO disruption (or SRO-disruption for Li-rich disordered rocksalt cathodes) must be completed as early as possible in the first charge, so that fast Li diffusion in the fully rejuvenated structure would allow for a high discharge capacity, comparable to the 1st-charge capacity. Indeed, the higher initial discharge capacity and Coulombic efficiency of 10M-N250 compared with N250 are consistent with accelerated "full" MRO-disruption upon first cycling after the thermal rejuvenation by the AMT-treatment (Figure S9). Note that as we discussed in Section 3.3, "rejuvenation by MRO/SRO-disruption" describes the so-called "Li_2MnO_3-activation" observed in the Li/Mn-rich layered cathodes. Thus, achieving efficient MRO disruption is equivalent to achieving "efficient Li_2MnO_3-activation" in the case of the layered Li/Mn-rich cathodes. In this context, any strategy that can facilitate MRO/SRO disruption would improve the performance of Li-rich layered/disordered-rocksalt cathodes. For example, it could be the thermal pretreatment (pre-activation) as we did for N125/N250 or doping of elements that could interrupt the MRO/SRO formation during material synthesis.[18,41,42,56−58] Interestingly, it was shown that the *C*2/*m*-MRO develops less in $0.5Li_2MnO_3{\cdot}0.5LiMn_{0.5-x}Ni_{0.5-x}Co_{2x}O_2$ cathodes with increasing cobalt content in the structure.[59] This trend suggests that Co^{3+}-doping effectively prerejuvenates the Li-rich layered cathodes by partially interrupting the *C*2/*m*-MRO formation during material synthesis, which may explain why Co-doped Li-rich layered cathodes typically deliver higher capacity with better initial Coulombic efficiency and rate capability compared with Co-free Li-rich layered cathodes.[8−10,59] Meanwhile, it must be noted that Li-rich and Mn-rich layered oxides may not necessarily develop a multi-domain structure through careful tuning of the material composition, which would help to improve performance in terms of both Li transport and structural reversibility upon O-redox.[11]

Another consideration would be the control of oxygen mobility in the Li-rich structure. As mentioned above, the reduced oxygen migration barrier upon O-redox (thus promoting LOM and LMM) facilitates the MRO/SRO disruption for improved Li-transport property. Ironically, the lowered oxygen diffusion barrier can also increase the GOM, triggering detrimental reactions near the particle surface, such as the O-loss, pore creation, and electrolyte decomposition.[19−21] In Figure 2d,e, we observe that voltage hysteresis of N125/N250 decreases upon cycling up to ∼20th cycle, and then, it starts increasing slowly. We believe that the earlier reduction of the hysteresis is due to the effect of LOM-driven MRO disruption (rejuvenation) on cycling kinetics being greater than that of the GOM-triggered side reactions. As the MRO disruption approaches near completion, the GOM-side reactions start dominating the evolution of the cycling kinetics, which explains the later increase in hysteresis.

In this context, the AMT-molten-salt treatment appears to be one of the ideal treatments for Li-rich cathodes. First of all, as we have shown for the first time in this paper, this treatment can thermally disturb the MRO to prerejuvenate (preactivate) the Li-rich materials in the interior to achieve improved performance (*e.g.*, higher 1st-cycle Coulombic efficiency, and higher capacity) and minimize the activation period (Figure S8). Also, high-temperature Li- and O-leaching and the continuous concentration-gradient structure generated by this treatment can mitigate the GOM-related structural damages, stabilizing the cycling performance.[21] Indeed, it is impressive to see as little as ∼4% capacity loss from 10M-N250 upon 200 cycles at 100 mA/g and that the material can deliver as high as 154 mA h/g-capacity even at 10C-rate (2 A/g). Finally, the average discharge voltage of 10M-N250 decreases only by ∼140 mV (from 3.65 to 3.51 V) during 200 cycles at 100 mA/g (Figure S11), which is remarkably small considering that various Li-rich cathodes have shown significantly greater voltage decay sometimes, up to more than 600 mV upon 100 cycles.[8−10] These results reveal how facilitating the rejuvenation process while mitigating GOM can improve the performance of Li-rich cathodes. We believe that further study on the rejuvenation process in Li-rich crystals with various structures (*e.g.*, layered, disordered) and the development of high-temperature prerejuvenation methods would help us to design high-performing and sustainable cathodes for Li-ion batteries.

4. CONCLUSIONS

In conclusion, based on the study of highly Li-rich layered- and disordered-rocksalt cathodes, we revealed that, in stark contrast to the current wisdom, the oxygen-redox-assisted structural change can be beneficial to the performance of the Li-rich cathodes by disrupting the local charge order and increasing the crystal volume, which substantially improves the Li-transport property in the materials. While the GOM promoted upon O-redox should be prevented because it leads to irreversible O-loss or side-reactions with the electrolytes, the LOM and associated TM disordering should be promoted, such that the fully rejuvenated Li-rich cathodes can achieve high capacity, high rate capability, and high Coulombic efficiency through the improved Li-transport property. We believe that our mechanistic understanding of the local-charge-order disruption and its influence on the Li-transport property, as well as the demonstration of high-performing Co-free layered cathodes, will pave an exciting new route to the development of sustainable and high-energy Li-ion batteries.

https://dx.doi.org/10.1021/acsaem.0c01315
ACS Appl. Energy Mater. 2020, 3, 7931−7943

■ ASSOCIATED CONTENT

Supporting Information

The Supporting Information is available free of charge at https://pubs.acs.org/doi/10.1021/acsaem.0c01315.

XRD and XPS analysis of the N125 and N250 powder/electrode samples; XRD, SEM, and energy-dispersive X-ray spectroscopy analysis of the molten salt process; STEM-images of the 10M-N250 focused-ion-beamed sample; discharge capacity and voltage-hysteresis analysis of N250, 5M-N250, and 10M-N250 samples; electrochemical data of N125 and 10M-N125 samples; and voltage retention data of 5M- and 10M-N250 samples (PDF)

■ AUTHOR INFORMATION

Corresponding Author

Ju Li − *Department of Nuclear Science and Engineering and Department of Materials Science and Engineering, Massachusetts Institute of Technology, Cambridge, Massachusetts 02139, United States;* orcid.org/0000-0002-7841-8058; Email: liju@mit.edu

Authors

Jinhyuk Lee − *Department of Nuclear Science and Engineering, Massachusetts Institute of Technology, Cambridge, Massachusetts 02139, United States;* orcid.org/0000-0001-5705-6513

Daiwei Yu − *Department of Electrical Engineering and Computer Science, Massachusetts Institute of Technology, Cambridge, Massachusetts 02139, United States*

Zhi Zhu − *Department of Nuclear Science and Engineering, Massachusetts Institute of Technology, Cambridge, Massachusetts 02139, United States*

Xiahui Yao − *Department of Nuclear Science and Engineering, Massachusetts Institute of Technology, Cambridge, Massachusetts 02139, United States;* orcid.org/0000-0001-6258-2382

Chao Wang − *Department of Nuclear Science and Engineering, Massachusetts Institute of Technology, Cambridge, Massachusetts 02139, United States;* orcid.org/0000-0002-8369-927X

Yanhao Dong − *Department of Nuclear Science and Engineering, Massachusetts Institute of Technology, Cambridge, Massachusetts 02139, United States*

Rahul Malik − *CAMX Power LLC, Lexington, Massachusetts 02421, United States*

Complete contact information is available at: https://pubs.acs.org/10.1021/acsaem.0c01315

Notes

The authors declare no competing financial interest.

■ ACKNOWLEDGMENTS

We acknowledge the support from Wuxi Weifu High Technology Group Co., Ltd.

■ REFERENCES

(1) Li, M.; Lu, J. Cobalt in Lithium-ion batteries. *Science* **2020**, *367*, 979−980.

(2) Dai, K.; Wu, J.; Zhuo, Z.; Li, Q.; Sallis, S.; Mao, J.; Ai, G.; Sun, C.; Li, Z.; Gent, W. E.; Chueh, W. C.; Chuang, Y.-d.; Zeng, R.; Shen, Z.-x.; Pan, F.; Yan, S.; Piper, L. F. J.; Hussain, Z.; Liu, G.; Yang, W. High Reversibility of Lattice Oxygen Redox Quantified by Direct Bulk Probes of Both Anionic and Cationic Redox Reaction. *Joule* **2019**, *3*, 518−541.

(3) Xu, Y.; Hu, E.; Yang, F.; Corbett, J.; Sun, Z.; Lyu, Y.; Yu, X.; Liu, Y.; Yang, X.-Q.; Li, H. Structural integrity−searching the key factor to suppress the voltage fade of Li-rich layered cathode materials through 3D X-ray imaging and spectroscopy techniques. *Nano Energy* **2016**, *28*, 164−171.

(4) Freire, M.; Kosova, N. V.; Jordy, C.; Chateigner, D.; Lebedev, O. I.; Maignan, A.; Pralong, V. A new actice Li-Mn-O compound for high energy density Li-ion batteries. *Nat. Mater.* **2016**, *15*, 173−177.

(5) Lee, J.; Kitchaev, D. A.; Kwon, D.-H.; Lee, C.-W.; Papp, J. K.; Liu, Y.-S.; Lun, Z.; Clément, R. J.; Shi, T.; McCloskey, B. D.; Guo, J.; Balasubramanian, M.; Ceder, G. Reversible Mn^{2+}/Mn^{4+} double redox in lithium-excess cathode materials. *Nature* **2018**, *556*, 185−190.

(6) Yabuuchi, N.; Takeuchi, M.; Nakayama, M.; Shiiba, H.; Ogawa, M.; Nakayama, K.; Ohta, T.; Endo, D.; Ozaki, T.; Inamasu, T.; Sato, K.; Komaba, S. High-capacity electrode materials for rechargeable lithium batteries: Li_3NbO_4-based system with cation-disordered rocksalt structure. *Proc. Natl. Acad. Sci. U.S.A.* **2015**, *112*, 7650−7655.

(7) Lu, Z.; MacNeil, D. D.; Dahn, J. R. Layered $Li[Ni_xCo_{1-2x}Mn_x]O_2$ cathode materials for lithium-ion batteries. *Electrochem. Solid-State Lett.* **2001**, *4*, A200−A203.

(8) Thackeray, M. M.; Kang, S.-H.; Johnson, C. S.; Vaughey, J. T.; Benedek, R.; Hackney, S. A. Li_2MnO_3-stabilized $LiMO_2$ (M = Mn, Ni, Co) electrodes for lithium-ion batteries. *J. Mater. Chem.* **2007**, *17*, 3112−3125.

(9) Lee, W.; Muhammad, S.; Sergey, C.; Lee, H.; Yoon, J.; Kang, Y.-M.; Yoon, W.-S. Advances in the cathode materials for lithium rechargeable batteries. *Angew. Chem., Int. Ed.* **2020**, *59*, 2578−2605.

(10) Manthiram, A.; Knight, J. C.; Myung, S.-T.; Oh, S.-M.; Sun, Y.-K. Nickel-rich and lithium-rich layered oxide cathodes: progress and perspectives. *Adv. Energy Mater.* **2016**, *6*, 1501010.

(11) Zhao, E.; Zhang, M.; Wang, X.; Hu, E.; Liu, J.; Yu, X.; Olguin, M.; Wynn, T. A.; Meng, Y. S.; Page, K.; Wang, F.; Li, H.; Yang, X.-Q.; Huang, X.; Chen, L. Local structure adaptability through multi cations for oxygen redox accommodation in Li-rich layered oxides. *Energy Storage Mater.* **2020**, *24*, 384−393.

(12) Zhao, E.; He, L.; Wang, B.; Li, X.; Zhang, J.; Wu, Y.; Chen, J.; Zhang, S.; Liang, T.; Chen, Y.; Yu, X.; Li, H.; Chen, L.; Huang, X.; Chen, H.; Wang, F. Structural and mechanistic revelations on high capacity cation-disordered Li-rich oxides for rechargeable Li-ion batteries. *Energy Storage Mater.* **2019**, *16*, 354−363.

(13) Luo, K.; Roberts, M. R.; Hao, R.; Guerrini, N.; Pickup, D. M.; Liu, Y.-S.; Edström, K.; Guo, J.; Chadwick, A. V.; Duda, L. C.; Bruce, P. G. Charge-compensation in 3d-transition-metal-oxide intercalation cathodes through the generation of localized electron holes on oxygen. *Nat. Chem.* **2016**, *8*, 684−691.

(14) Seo, D.-H.; Lee, J.; Urban, A.; Malik, R.; Kang, S.; Ceder, G. The structural and chemical origin of the oxygen redox activity in layered and cation-disordered Li-excess cathode materials. *Nat. Chem.* **2016**, *8*, 692−697.

(15) Bréger, J.; Dupré, N.; Chupas, P. J.; Lee, P. L.; Proffen, T.; Parise, J. B.; Grey, C. P. Short-and long-range order in the positive electrode material, $Li(NiMn)_{0.5}O_2$: a joint X-ray and neutron diffraction, pair distribution function analysis and NMR study. *J. Am. Chem. Soc.* **2005**, *127*, 7529.

(16) Jones, M. A.; Reeves, P. J.; Seymour, I. D.; Cliffe, M. J.; Dutton, S. E.; Grey, C. P. Short-range ordering in a battery electrode, the "cation-disordered" rocksalt $Li_{1.25}Nb_{0.25}Mn_{0.5}O_2$. *Chem. Commun.* **2019**, *55*, 9027−9030.

(17) Huang, Y.; Liu, L.; Zhu, Y.; Gao, M.; Zhang, J. A new model on cation distribution in cation-disordered $Li_{1+x}TM_{1-x}O_2$ cathodes. *Solid State Ionics* **2020**, *351*, 115341.

(18) Ji, H.; Urban, A.; Kitchaev, D. A.; Kwon, D.-H.; Artrith, N.; Ophus, C.; Huang, W.; Cai, Z.; Shi, T.; Kim, J. C.; Kim, H.; Ceder, G. Hidden structural and chemical order controls lithium transport in cation-disordered oxides for rechargeable batteries. *Nat. Commun.* **2019**, *10*, 592.

(19) Myeong, S.; Cho, W.; Jin, W.; Hwang, J.; Yoon, M.; Yoo, Y.; Nam, G.; Jang, H.; Hang, J.-G.; Choi, N.-S.; Kim, M. G.; Cho, J. Understanding voltage decay in lithium-excess layered cathode materials through oxygen-centred structural arrangement. *Nat. Commun.* **2018**, *9*, 3285.

(20) Hu, E.; Yu, X.; Lin, R.; Bi, X.; Lu, J.; Bak, S.; Nam, K.-W.; Xin, H. L.; Jaye, C.; Fischer, D. A.; Amine, K.; Yang, X.-Q. Evolution of redox couples in Li- and Mn-rich cathode materials and mitigation of voltage fade by reducing oxygen release. *Nat. Energy* **2018**, *3*, 690−698.

(21) Zhu, Z.; Yu, D.; Yang, Y.; Su, C.; Huang, Y.; Dong, Y.; Waluyo, I.; Wang, B.; Hunt, A.; Yao, X.; Lee, J.; Xue, W.; Li, J. Gradient Li-rich oxide cathode particles immunized against oxygen release by a molten salt treatment. *Nat. Energy* **2019**, *4*, 1049−1058.

(22) House, R. A.; Maitra, U.; Pérez-Osorio, M. A.; Lozano, J. G.; Jin, L.; Somerville, J. W.; Duda, L. C.; Nag, A.; Walters, A.; Zhou, K.-J.; Roberts, M. R.; Bruce, P. G. Superstructure control of first-cycle voltage hysteresis in oxygen-redox cathodes. *Nature* **2020**, *577*, 502−508.

(23) Chen, G.; An, J.; Meng, Y.; Yuan, C.; Matthews, B.; Dou, F.; Shi, L.; Zhou, Y.; Song, P.; Wu, G.; Zhang, D. Cation and anion Co-doping synergy to improve structural stability of Li- and Mn-rich layered cathode materials for lithium-ion batteries. *Nano Energy* **2019**, *57*, 157−165.

(24) Lee, H.; Lim, S. B.; Kim, J. Y.; Jeong, M.; Park, Y. J.; Yoon, W.-S. Characterization and control of irreversible reaction in Li-rich cathode during the initial charging process. *ACS Appl. Mater. Interfaces* **2018**, *10*, 10804−10818.

(25) Lee, J.; Papp, J. K.; Clément, R. J.; Sallis, S.; Kwon, D.-H.; Shi, T.; Yang, W.; McCloskey, B. D.; Ceder, G. Mitigating oxygen loss to improve the cycling performance of high capacity cation-disordered cathode materials. *Nat. Commun.* **2017**, *8*, 981.

(26) Eum, D.; Kim, B.; Kim, S. J.; Park, H.; Wu, J.; Cho, S.-P.; Yoon, G.; Lee, M. H.; Jung, S.-K.; Yang, W.; Seong, W. M.; Ku, K.; Tamwattana, O.; Park, S. K.; Hwang, I.; Kang, K. Voltage decay and redox asymmetry mitigation by reversible cation migration in lithium-rich layered oxide electrodes. *Nat. Mater.* **2020**, *19*, 419−427.

(27) Oh, P.; Ko, M.; Myeong, S.; Kim, Y.; Cho, J. A novel surface treatment method and new insight into discharge voltage deterioration for high-performance $0.4Li_2MnO_3$-$0.6LiNi_{1/3}Co_{1/3}Mn_{1/3}O_2$ cathode materials. *Adv. Energy Mater.* **2014**, *4*, 1400631.

(28) Liu, S.; Liu, Z.; Shen, X.; Wang, X.; Liao, S.-C.; Yu, R.; Wang, Z.; Hu, Z.; Chen, C.-T.; Yu, X.; Yang, X.; Chen, L. Li−Ti cation mixing enhanced structural stability of Li-rich layered oxide. *Adv. Energy Mater.* **2019**, *9*, 1901530.

(29) Zheng, J.; Gu, M.; Xiao, J.; Polzin, B. J.; Yan, P.; Chen, X.; Wang, C.; Zhang, J.-G. Functioning mechanism of AlF_3 coating on the Li- and Mn-rich cathode materials. *Chem. Mater.* **2014**, *26*, 6320−6327.

(30) Zhang, X.; Xie, X.; Yu, R.; Zhou, J.; Huang, Y.; Cao, S.; Wang, Y.; Tang, K.; Wu, C.; Wang, X. Improvement of the cycling stability of Li-rich layered Mn-based oxides cathodes modified by nanoscale $LaPO_4$ coating. *ACS Appl. Energy Mater.* **2019**, *2*, 3532−3541.

(31) Fu, Z.; Hu, J.; Hu, W.; Yang, S.; Luo, Y. Quantitative analysis of Ni^{2+}/Ni^{3+} in $Li[Ni_xMn_yCo_z]O_2$ cathode materials: non-linear least-squares fitting of XPS spectra. *Appl. Surf. Sci.* **2018**, *441*, 1048−1056.

(32) Armstrong, A. R.; Holzapfel, M.; Novák, P.; Johnson, C. S.; Kang, S.-H.; Thackeray, M. M.; Bruce, P. G. Demonstrating oxygen loss and associated structural reorganization in the lithium battery cathode. *J. Am. Chem. Soc.* **2006**, *128*, 8694−8698.

(33) Xu, J.; Sun, M.; Qiao, R.; Renfrew, S. E.; Ma, L.; Wu, T.; Hwang, S.; Nordlund, D.; Su, D.; Amine, K.; Lu, J.; McCloskey, B. D.; Yang, W.; Tong, W. Elucidating anionic oxygen activity in lithium-rich layered oxides. *Nat. Commun.* **2018**, *9*, 947.

(34) Liu, W.; Oh, P.; Liu, X.; Lee, M.-J.; Cho, W.; Chae, S.; Kim, Y.; Cho, J. Nickel-rich layered lithium transition-metal oxide for high-energy lithium-ion batteries. *Angew. Chem., Int. Ed.* **2015**, *54*, 4440.

(35) Hong, J.; Seo, D.-H.; Kim, S.-W.; Gwon, H.; Oh, S.-T.; Kang, K. Structural evolution of layered $Li_{1.2}Ni_{0.2}Mn_{0.6}O_2$ upon electrochemical cycling in a Li rechargeable battery. *J. Mater. Chem.* **2010**, *20*, 10179−10186.

(36) Ates, M. N.; Mukerjee, S.; Abraham, K. M. A high rate Li-rich layered MNC cathode for lithium-ion batteries. *RSC Adv.* **2015**, *5*, 27375−27386.

(37) Li, Y.; Bettge, M.; Polzin, B.; Zhu, Y.; Balasubramanian, M.; Abraham, D. P. Understanding long-term performance of $Li_{1.2}Ni_{0.15}Mn_{0.55}Co_{0.1}O_2$−graphite lithium-ion cells. *J. Electrochem. Soc.* **2013**, *160*, A3006−A3019.

(38) Sollich, P. Rheological constitutive equation for a model of soft glassy materials. *Phys. Rev. E: Stat. Phys., Plasmas, Fluids, Relat. Interdiscip. Top.* **1998**, *58*, 738−759.

(39) Viasnoff, V.; Lequeux, F. Rejuvenation and overaging in a colloidal glass under shear. *Phys. Rev. Lett.* **2002**, *89*, 065701.

(40) Bursac, P.; Lenormand, G.; Fabry, B.; Oliver, M.; Weitz, D. A.; Viasnoff, V.; Butler, J. P.; Fredberg, J. J. Cytoskeletal remodeling and slow dynamics in the living cell. *Nat. Mater.* **2005**, *4*, 557−561.

(41) Kang, S.-H.; Johnson, C. S.; Vaughey, J. T.; Amine, K.; Thackeray, M. M. The effects of acid treatment on the electrochemical properties of 0.5 Li_2MnO_3•0.5 $LiNi_{0.44}Co_{0.25}Mn_{0.31}O_2$ electrodes in lithium cells. *J. Electrochem. Soc.* **2006**, *153*, A1186−A1192.

(42) Zheng, J.; Deng, S.; Shi, Z.; Xu, H.; Deng, Y.; Zhang, Z.; Chen, G. The effects of persulfate treatment on the electrochemical properties of $Li[Li_{0.2}Mn_{0.54}Ni_{0.13}Co_{0.13}]O_2$. *J. Power Sources* **2013**, *221*, 108−113.

(43) Weppner, W.; Huggins, R. A. Determination of the kinetic parameters of mixed-conducting electrodes and application to the system Li_3Sb. *J. Electrochem. Soc.* **1977**, *124*, 1569−1578.

(44) Lee, J.; Seo, D.-H.; Balasubramanian, M.; Twu, N.; Li, X.; Ceder, G. A new class of high capacity cation-disordered oxides for rechargeable lithium batteries: Li−Ni−Ti−Mo oxides. *Energy Environ. Sci.* **2015**, *8*, 3255−3265.

(45) Song, B.; Liu, H.; Liu, Z.; Xiao, P.; Lai, M. O.; Lu, L. High rate capability caused by surface cubic spinels in Li-rich layer-structured cathodes for Li-ion batteries. *Sci. Rep.* **2013**, *3*, 3094.

(46) Li, L.; Wang, L.; Zhang, X.; Xue, Q.; Wei, L.; Wu, F.; Chen, R. 3D reticular $Li_{1.2}Ni_{0.2}Mn_{0.6}O_2$ cathode material for lithium-ion batteries. *ACS Appl. Mater. Interfaces* **2017**, *9*, 1516−1523.

(47) Aydinol, M. K.; Kohan, A. F.; Ceder, G.; Cho, K.; Joannopoulos, J. Ab initio study of lithium intercalation in metal oxides and metal dichalcogenides. *Phys. Rev. B: Condens. Matter Mater. Phys.* **1997**, *56*, 1353−1365.

(48) Jain, A.; Ong, S. P.; Hautier, G.; Chen, W.; Richards, W. D.; Dacek, S.; Cholia, S.; Gunter, D.; Skinner, D.; Ceder, G.; Persson, K. Commentary: The Materials Project: A materials genome approach to accelerating materials innovation. *APL Mater.* **2013**, *1*, 011002.

(49) Kang, K.; Meng, Y. S.; Bréger, J.; Grey, C. P.; Ceder, G. Electrodes with high power and high capacity for rechargeable lithium batteries. *Science* **2006**, *311*, 977−980.

(50) Lee, J.; Urban, A.; Li, X.; Su, D.; Hautier, G.; Ceder, G. Unlocking the potential of cation-disordered oxides for rechargeable lithium batteries. *Science* **2014**, *343*, 519−522.

(51) Nakajima, M.; Yabuuchi, N. Lithium-excess cation-disordered rocksalt-type oxide with nanoscale phase segregation: $Li_{1.25}Nb_{0.25}V_{0.5}O_2$. *Chem. Mater.* **2017**, *29*, 6927−6935.

(52) Lee, E.; Persson, K. A. Structural and chemical evolution of the layered Li-excess Li_xMnO_3 as a function of Li content from first-principles calculations. *Adv. Energy Mater.* **2014**, *4*, 1400498.

(53) Gent, W. E.; Lim, K.; Liang, Y.; Li, Q.; Barnes, T.; Ahn, S.-J.; Stone, K. H.; McIntire, M.; Hong, J.; Song, J. H.; Li, Y.; Mehta, A.; Ermon, S.; Tyliszcak, T.; Kilcoyne, D.; Vine, D.; Park, J.-H.; Doo, S.-K.; Toney, M. F.; Yang, W.; Prendergast, D.; Chueh, W. C. Coupling between oxygen redox and cation migration explains unusual electrochemistry in lithium-rich layered oxides. *Nat. Commun.* **2017**, *8*, 2091.

(54) Chen, H.; Islam, M. S. Lithium extraction mechanism in Li-rich Li_2MnO_3 involving oxygen hole formation and dimerization. *Chem. Mater.* **2016**, *28*, 6656−6663.

https://dx.doi.org/10.1021/acsaem.0c01315
ACS Appl. Energy Mater. 2020, 3, 7931−7943

(55) Croy, J. R.; Iddir, H.; Gallagher, K.; Johnson, C. S.; Benedek, R.; Balasubramanian, M. First-charge instabilities of layered-layered lithium-ion battery materials. *Phys. Chem. Chem. Phys.* **2015**, *17*, 24382−24391.

(56) Wang, M.-J.; Shao, A.-F.; Yu, F.-D.; Sun, G.; Gu, D.-M.; Wang, Z.-B. Simple water treatment strategy to optimnize the Li_2MnO_3 activation of lithium-rich cathode materials. *ACS Sustainable Chem. Eng.* **2019**, *7*, 12825−12837.

(57) Wang, M.-J.; Yu, F.-D.; Sun, G.; Gu, D.-M.; Wang, Z.-B. Optimizing the structural evolution of Li-rich oxide cathode materials via microwave-assisted pre-activation. *ACS Appl. Energy Mater.* **2018**, *1*, 4158−4168.

(58) Shi, J.-L.; Xiao, D.-D.; Ge, M.; Yu, X.; Chu, Y.; Huang, X.; Zhang, X.-D.; Yin, Y.-X.; Yang, X.-Q.; Guo, Y.-G.; Gu, L.; Wan, L.-J. High-capacity cathode material with high voltage for Li-ion batteries. *Adv. Mater.* **2018**, *30*, 1705575.

(59) Wu, Y.; Xie, L.; He, X.; Zhuo, L.; Wang, L.; Ming, J. Electrochemical activation, voltage decay and hysteresis of Li-rich layered cathode probed by various cobalt content. *Electrochim. Acta* **2018**, *265*, 115−120.

https://dx.doi.org/10.1021/acsaem.0c01315
ACS Appl. Energy Mater. 2020, 3, 7931−7943

Supporting Information

Kinetic Rejuvenation of Li-Rich Li-Ion Battery Cathodes upon Oxygen Redox

Jinhyuk Lee[1,5], Daiwei Yu[2], Zhi Zhu[1], Xiahui Yao[1], Chao Wang[1], Yanhao Dong[1], Rahul Malik[4], Ju Li[1,3*]

[1] Department of Nuclear Science and Engineering, Massachusetts Institute of Technology, Cambridge, MA 02139, USA

[2] Department of Electrical Engineering and Computer Science, Massachusetts Institute of Technology, Cambridge, MA 02139, USA

[3] Department of Materials Science and Engineering, Massachusetts Institute of Technology, Cambridge, MA 02139, USA

[4]CAMX Power LLC, Lexington, MA 02421, USA

[5] Present address: Department of Mining and Materials Engineering, McGill University, Montréal, QC H3A 0C5, Canada

[*]Email: liju@mit.edu

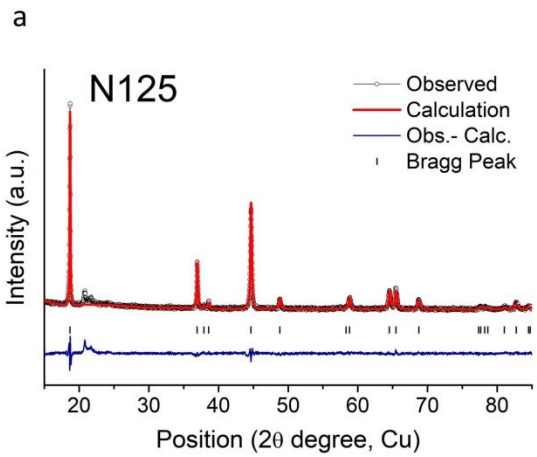

b

Space group: R-3m		(*u*,*v*,*w*) = (0.052863, 0.071513, 0.002574)				
Atom	**Wyckoff position**	***x***	***y***	***z***	**Occupancy**	**B_{iso}**
Li1	3a	0	0	0	1	0.5
Ni1	3a	0	0	0	0	0.5
Li2	3b	0	0	0.5	0.250	0.5
Ni2	3b	0	0	0.5	0.125	0.5
Mn2	3b	0	0	0.5	0.625	0.5
O1	6c	0	0	0.2422(5)	1	1.0
a=*b*=2.8491(7)Å		*c*=14.2318(9)Å		volume=100.0531Å^3		
R_{wp}=3.46597, Goodness of fit=2.5991						

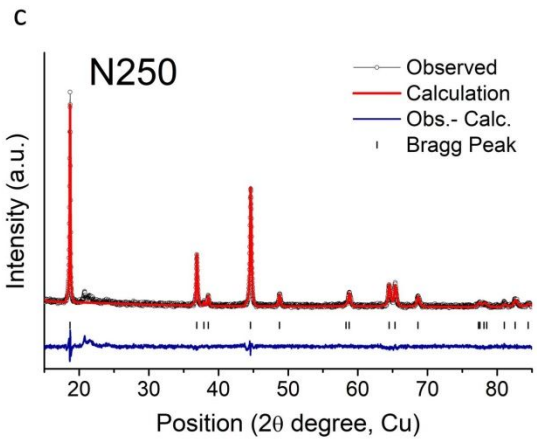

d

Space group: R-3m		(*u*,*v*,*w*) = (0.253554, -0.059170, 0.021622)				
Atom	**Wyckoff position**	***x***	***y***	***z***	**Occupancy**	**B_{iso}**
Li1	3a	0	0	0	0.96	0.5
Ni1	3a	0	0	0	0.0433	0.5
Li2	3b	0	0	0.5	0.2502	0.5
Ni2	3b	0	0	0.5	0.2094	0.5
Mn2	3b	0	0	0.5	0.5	0.5
O1	6c	0	0	0.2418(2)	1	1.0
a=*b*=2.8539(5)Å		*c*=14.2316(1)Å		volume=100.387Å^3		
R_{wp}=3.38719, Goodness of fit=1.90047						

Figure S1. The XRD refinement results and structural parameters of (a, b) $Li_{1.25}Ni_{0.125}Mn_{0.625}O_2$ (N125) and (c, d) $Li_{1.25}Ni_{0.250}Mn_{0.500}O_2$ (N250). The crystallographic information file of R-3m $LiNiO_2$ (ICSD collection code 78687) was used as an input file. Pseudo Voigt fit was used. The atomic occupancies were initially set to the atomic ratio obtained from elemental analysis, based on which the lattice parameters were first refined. Then, we further refined the lattice parameters and the atomic occupancies simultaneously: transition metal (TM) occupancies were first refined, and then Li occupancy was refined. To account for cation mixing between the Li- and TM-layer, we introduced Ni in the 3a site (Li-layer). However, a very similar refinement result can be obtained even if we let Mn in the 3a site instead of Ni. Thus, we cannot specify which TM is in the Li-layer.

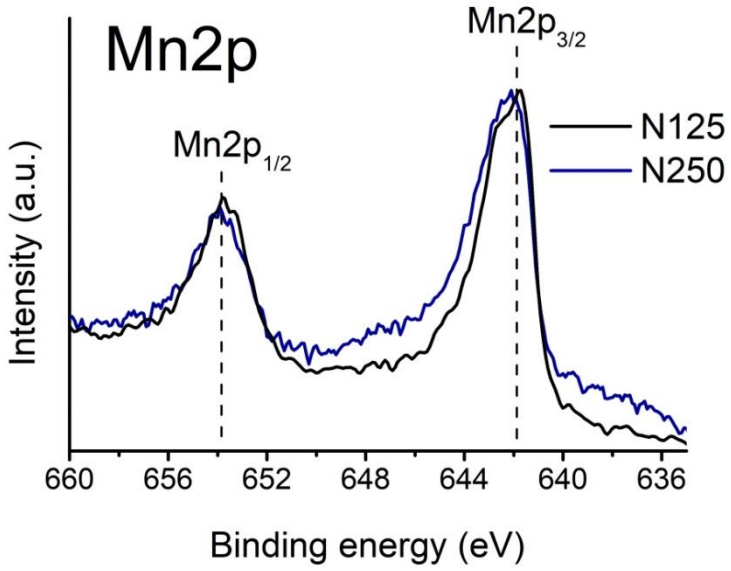

Figure S2. The Mn X-ray photoelectron spectroscopy result of the N125 and N250 powder samples. From both samples, we observe the binding energies of the Mn $2p_{3/2}$ and $2p_{1/2}$ at ~654 eV, and ~ 642 eV, which are the typical binding energies of Mn^{4+} such as in MnO_2.[1] This result indicates that the Mn in the as-made N125 and N250 is in the Mn^{4+} state.

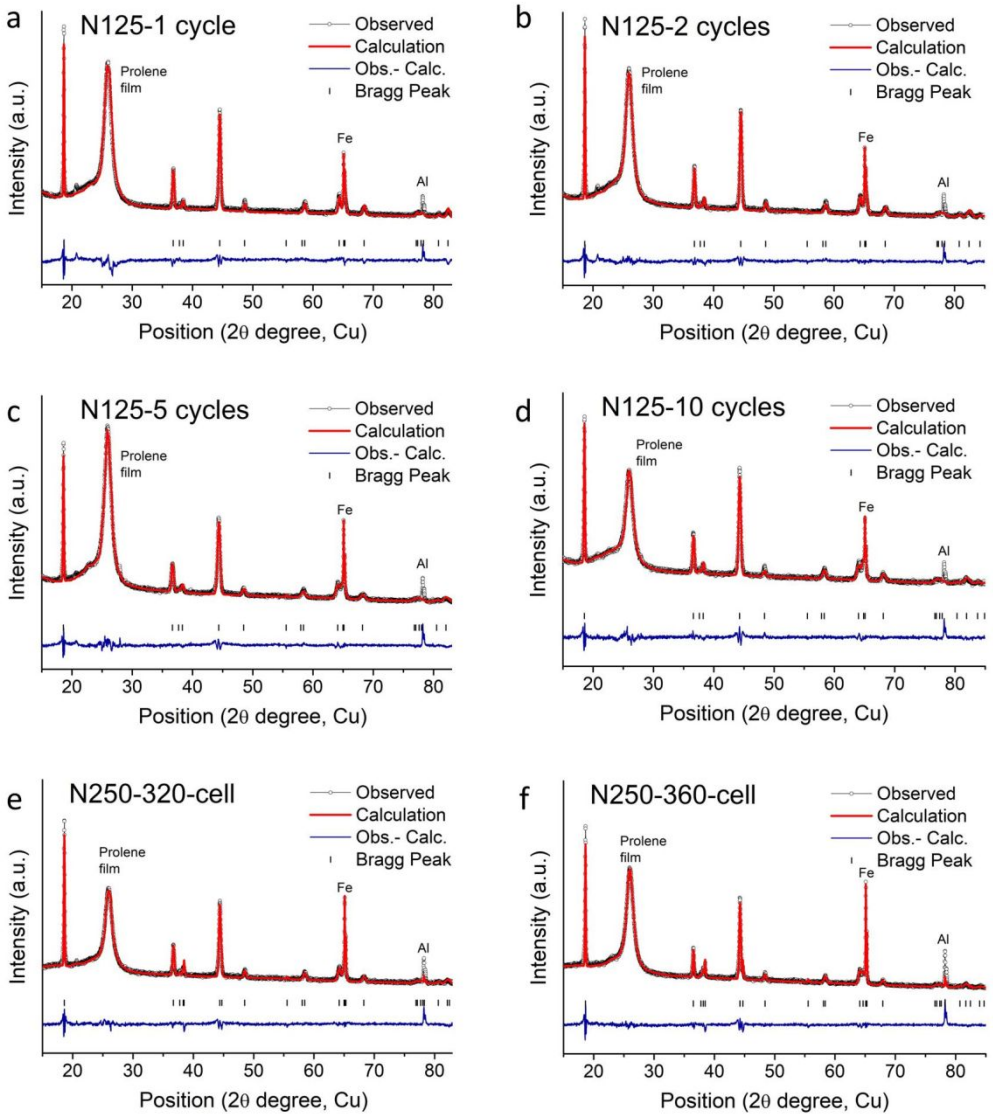

Figure S3. The XRD refinement results of the **(A, B, C, D)** N125 electrodes after 1, 2, 5, and 10 cycles between 2.0 V and 4.8 V at 20 mA/g and room temperature; and of the **(E, F)** N250 electrodes after the 1st cycle at 20 mA/g: for the N250-320-cell, N250 was charged to 320 mAh/g before the 1st discharging to 2.0 V (160 mAh/g-discharge) at room temperature. For the N250-360-cell, N250 was charged to 360 mAh/g at 60°C and then discharged to 2.0 V (230 mAh/g-discharged). The hump between the 25° to 28° is from the prolene film, which was applied to seal the electrode samples. The Fe peak is from the stainless steel XRD holder, and the Al peak is from the Al-current collector.

a

Space group: R-3m		(*u*,*v*,*w*) = (-0.634553, 0.854717, -0.092661)				
Atom	**Wyckoff position**	***x***	***y***	***z***	**Occupancy**	**B_{iso}**
Li1	3a	0	0	0	0.95	0.5
Ni1	3a	0	0	0	0.049	0.5
Li2	3b	0	0	0.5	0.05	0.5
Ni2	3b	0	0	0.5	0.1285	0.5
Mn2	3b	0	0	0.5	0.625	0.5
O1	6c	0	0	0.2417(5)	1	1.0
a=*b*=2.8596(8) Å		*c*=14.2592(5) Å		volume=100.986 Å^3		
R_{wp}=4.77, Goodness of fit=8.064						

b

Space group: R-3m		(*u*,*v*,*w*) = (0.278555, 0.380907, -0.039379)				
Atom	**Wyckoff position**	***x***	***y***	***z***	**Occupancy**	**B_{iso}**
Li1	3a	0	0	0	0.91	0.5
Ni1	3a	0	0	0	0.0831	0.5
Li2	3b	0	0	0.5	0.09	0.5
Ni2	3b	0	0	0.5	0.1046	0.5
Mn2	3b	0	0	0.5	0.625	0.5
O1	6c	0	0	0.2430(1)	1	1.0
a=*b*=2.8588(1) Å		*c*= 14.2668(3) Å		volume=100.986 Å^3		
R_{wp}=4.0897, Goodness of fit=5.9580						

c

Space group: R-3m		(*u*,*v*,*w*) = (0.278555, 0.380907, -0.039379)				
Atom	**Wyckoff position**	***x***	***y***	***z***	**Occupancy**	**B_{iso}**
Li1	3a	0	0	0	0.90	0.5
Ni1	3a	0	0	0	0.1021	0.5
Li2	3b	0	0	0.5	0.06	0.5
Ni2	3b	0	0	0.5	0.1024	0.5
Mn2	3b	0	0	0.5	0.625	0.5
O1	6c	0	0	0.2448(4)	1	1.0
a=*b*=2.8692(4) Å		*c*=14.3092(2) Å		volume=102.02 Å^3		
R_{wp}=4.0507, Goodness of fit=5.603						

d

Space group: R-3m		(*u*,*v*,*w*) =(1.631452, -0.34773, 0.061901)				
Atom	**Wyckoff position**	***x***	***y***	***z***	**Occupancy**	**B_{iso}**
Li1	3a	0	0	0	0.81	0.5
Ni1	3a	0	0	0	0.1044	0.5
Li2	3b	0	0	0.5	0.09	0.5
Ni2	3b	0	0	0.5	0.1017	0.5
Mn2	3b	0	0	0.5	0.625	0.5
O1	6c	0	0	0.2411(3)	1	1.0
a=*b*=2.8737(5) Å		*c*=14.3329(8) Å		volume=102.51 Å^3		
R_{wp}=3.49, Goodness of fit=4.167						

e

Space group: R-3m		(*u*,*v*,*w*) = (0.530085, 0.106281, 0.003378)				
Atom	**Wyckoff position**	***x***	***y***	***z***	**Occupancy**	**B_{iso}**
Li1	3a	0	0	0	0.94	0.5
Ni1	3a	0	0	0	0.0508	0.5
Li2	3b	0	0	0.5	0	0.5
Ni2	3b	0	0	0.5	0.2633	0.5
Mn2	3b	0	0	0.5	0.50	0.5
O1	6c	0	0	0.2432(7)	1	1.0
a=*b*=2.8676(6) Å		*c*=14.2914(4) Å		volume=101.7798 Å^3		
R_{wp}=4.727, Goodness of fit=5.374						

f

Space group: R-3m		(*u*,*v*,*w*) = (0.747234, -0.151373, 0.037176)				
Atom	**Wyckoff position**	***x***	***y***	***z***	**Occupancy**	**B_{iso}**
Li1	3a	0	0	0	0.88	0.5
Ni1	3a	0	0	0	0.0798	0.5
Li2	3b	0	0	0.5	0	0.5
Ni2	3b	0	0	0.5	0.2736	0.5
Mn2	3b	0	0	0.5	0.50	0.5
O1	6c	0	0	0.2422(5)	1	1.0
a=*b*=2.8817(2) Å		*c*=14.2777(8) Å		volume=102.682 Å^3		
R_{wp}=5.841, Goodness of fit=7.676						

Table S1. The structural parameters from the XRD refinement data in Figure S3: (a) N125-1 cycle, (b) N125-2 cycles, (c) N125-5 cycles, (d) N125-10 cycles, (e) N250-320-cell, (f) N250-360-cell. We used a similar protocol, as we described for Supplementary Fig. 1 for this refinement. The Li-occupancy was estimated by subtracting the irreversible Li loss during cycling from the original Li content, which can be obtained by translating the difference between the cumulative charge (Li-extracted) and discharge (Li-inserted) capacities into the irreversible Li-loss.

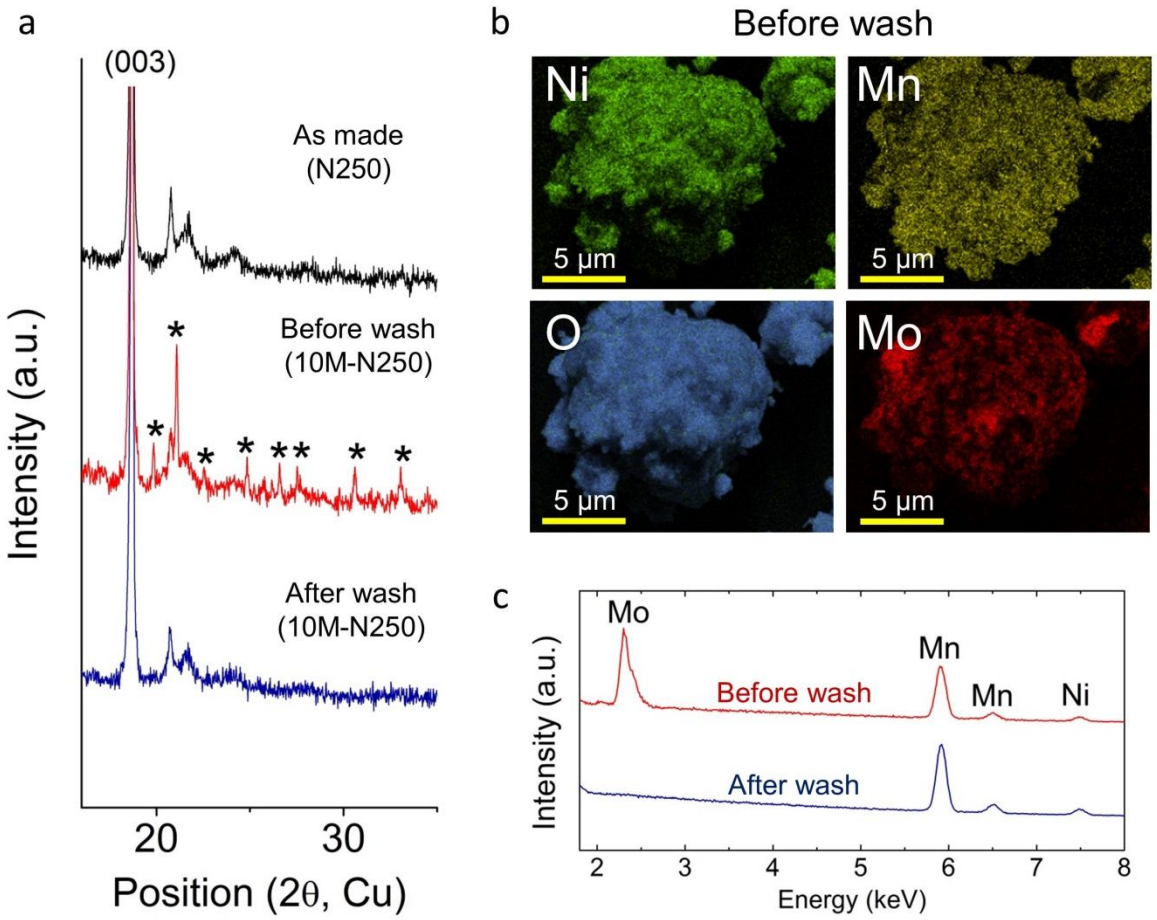

Figure S4. The molten-salt treatment procedure. (a) The XRD data from the as-made N250 powder (black), 10M-N250 powder before washing (red), and 10M-N250 powder (blue) after washing with the deionized water. The asterisks belong to the R3-Li_2MoO_4, which formed as a result of the Ammonium Molybdate Tetrahydrate (AMT) reacting with the as-made N250 powder to leach some lithium and oxygen from the N250 particles. The XRD peaks from Li_2MoO_4 are not seen after the washing. (b) The energy-dispersive X-ray spectroscopy (EDS) mapping on a "before wash" 10M-N250 particle. We can see the molybdenum signal from the particle surface, along with the signal from Ni, Mn, and O. (c) The EDS spectra of 10M-N250 particles before (red) and after wash (blue). From the spectra, we can see that the Mo signal disappears after the washing. These results confirm that the AMT-salt reacts with the N250 particles to form Li_2MoO_4, which is washed away with the deionized water. These results are consistent with our previous results.[2]

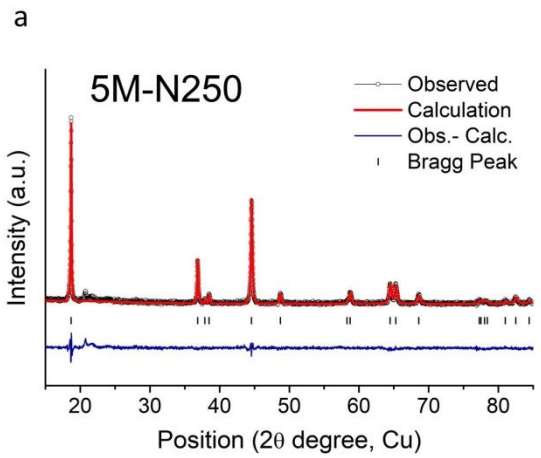

b

Space group: R-3m		(*u*,*v*,*w*) = (0.252517, -0.061149, 0.021234)				
Atom	**Wyckoff position**	***x***	***y***	***z***	**Occupancy**	**B_{iso}**
Li1	3a	0	0	0	0.95	0.5
Ni1	3a	0	0	0	0.045	0.5
Li2	3b	0	0	0.5	0.2917	0.5
Ni2	3b	0	0	0.5	0.2083	0.5
Mn2	3b	0	0	0.5	0.50	0.5
O1	6c	0	0	0.2422(2)	1	1.60
a=*b*=2.8564(9)Å		*c*=14.2353(1)Å			volume=100.592Å^3	
R_{wp}=3.323, Goodness of fit=1.8802						

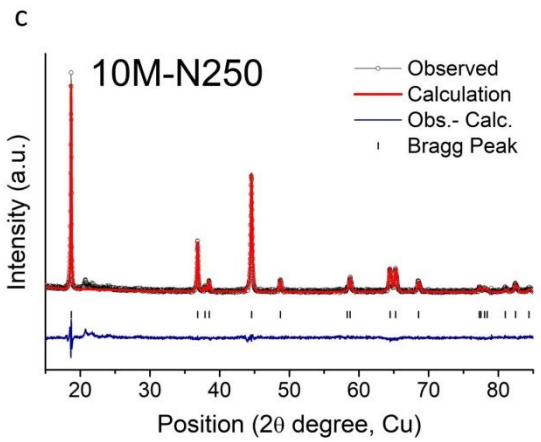

d

Space group: R-3m		(*u*,*v*,*w*) = (0.082412, 0.021972, 0.007181)				
Atom	**Wyckoff position**	***x***	***y***	***z***	**Occupancy**	**B_{iso}**
Li1	3a	0	0	0	0.96	0.5
Ni1	3a	0	0	0	0.038654	0.5
Li2	3b	0	0	0.5	0.24	0.5
Ni2	3b	0	0	0.5	0.2557	0.5
Mn2	3b	0	0	0.5	0.50	0.5
O1	6c	0	0	0.2414(3)	1	1.50
a=*b*=2.8582(5)Å		*c*=14.2403(9)Å			volume=100.7615Å^3	
R_{wp}=4.0647, Goodness of fit=2.872						

Figure S5. The XRD refinement results and structural parameters of (a, b) 5M-N250 and (c, d) 10M-N250. The protocol for this refinement was similar to the one described in Figure S1.

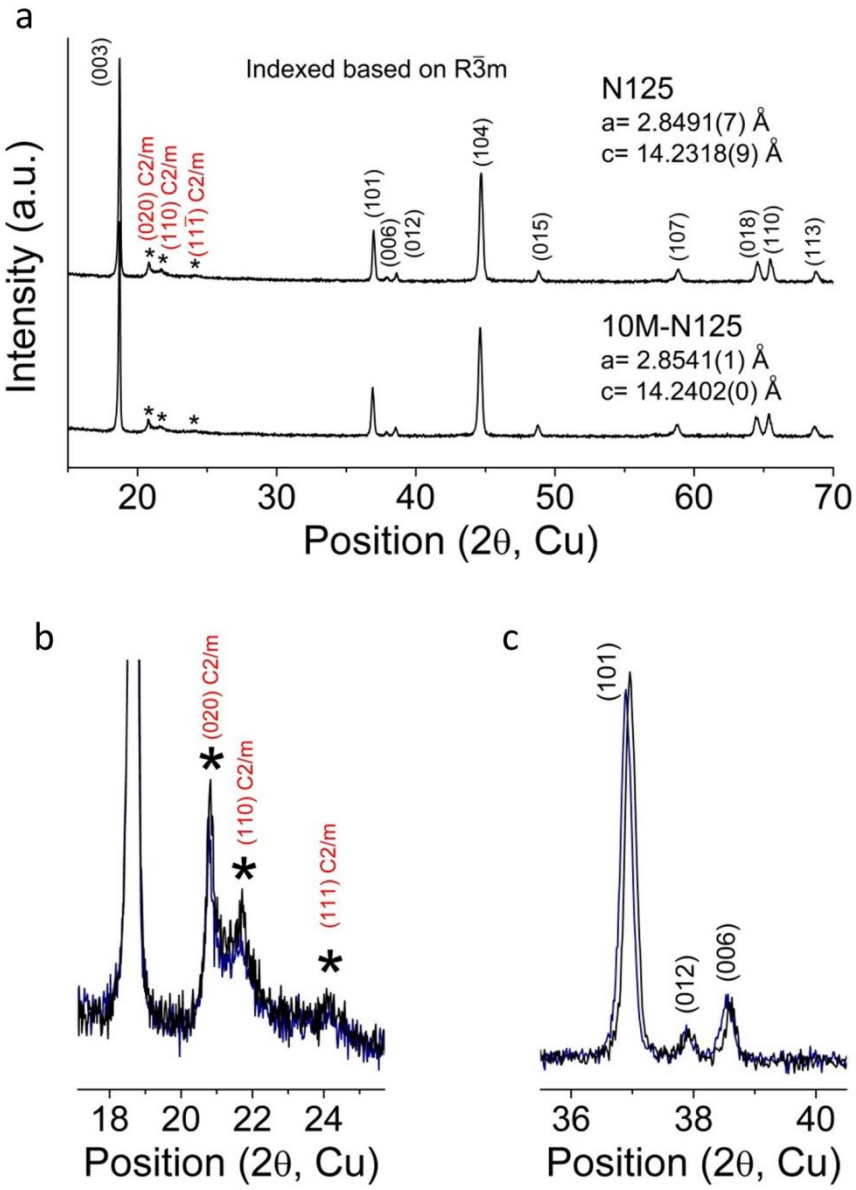

Figure S6. The structural change of N125 by the molten-salt treatment. (a) The XRD results of N125 and 10M-N125 powder samples. (b) The in-plane ordering XRD peaks from the N125 (black) and 10M-N125 (blue) samples. (c) The R-3m (101), (012), and (006) XRD peaks of the two samples. We observe that the in-plane ordering signals become weaker (*i.e.*, disturbance of the ordering), and the XRD peaks shift to lower angles (*i.e.*, volume increase) after the 10M-AMT treatment. This result shows that the AMT-treatment thermally disturbed the C2/m medium-range-order in the N125 structure, as was the case for N250.

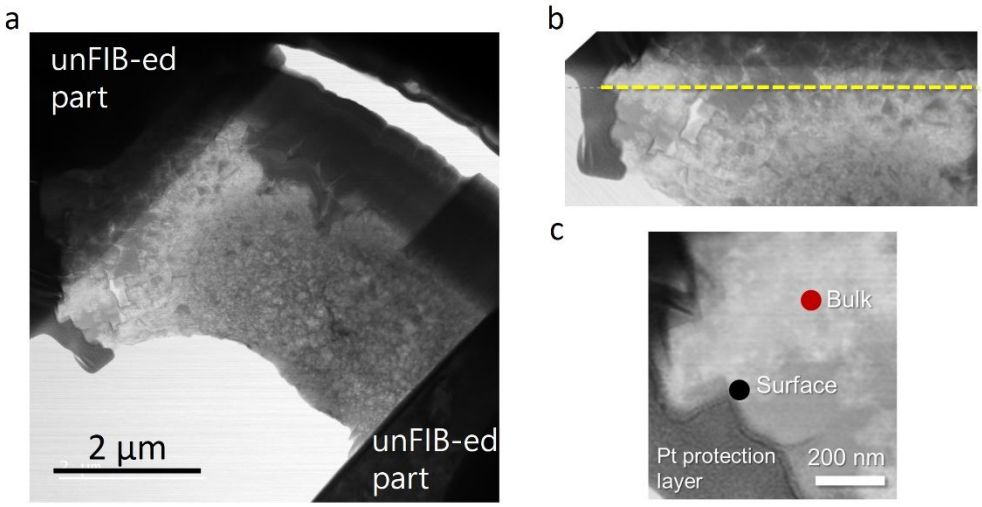

Figure S7. The morphology of the 10M-N250 focused-ion-beamed (FIB) sample used for the EELS measurement. (a) The scanning transmission electron microscopy (STEM) bright-field image of the FIB-ed 10M-N250 sample. The middle part of the image shows the FIB-ed portion. (b) The line-scan trajectory (yellow dash-line) during the EELS measurement. The EELS data shown the Figure 4b in the manuscript were collected from the two points in the image (c): the thickness of the portion shown in Figure c is ~90 nm.

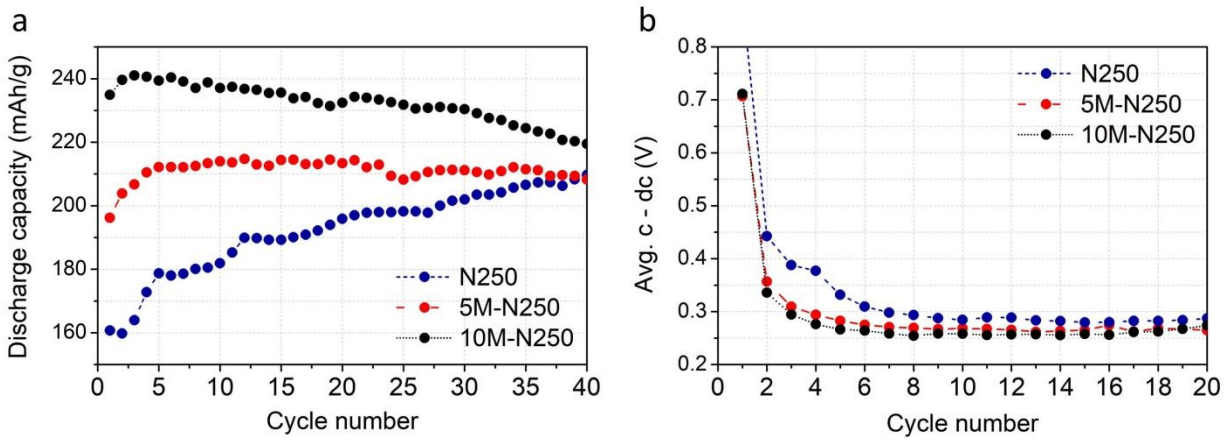

Figure S8. The shortened electrochemical rejuvenation period after the thermal pre-rejuvenation. (a) The discharge capacities of N250, 5M-N250, and 10M-N250 when they are cycled between 2.0 V and 4.8 V at 20 mA/g. (b) The difference between the average charging voltage and discharging voltage of the three materials during the cycle.

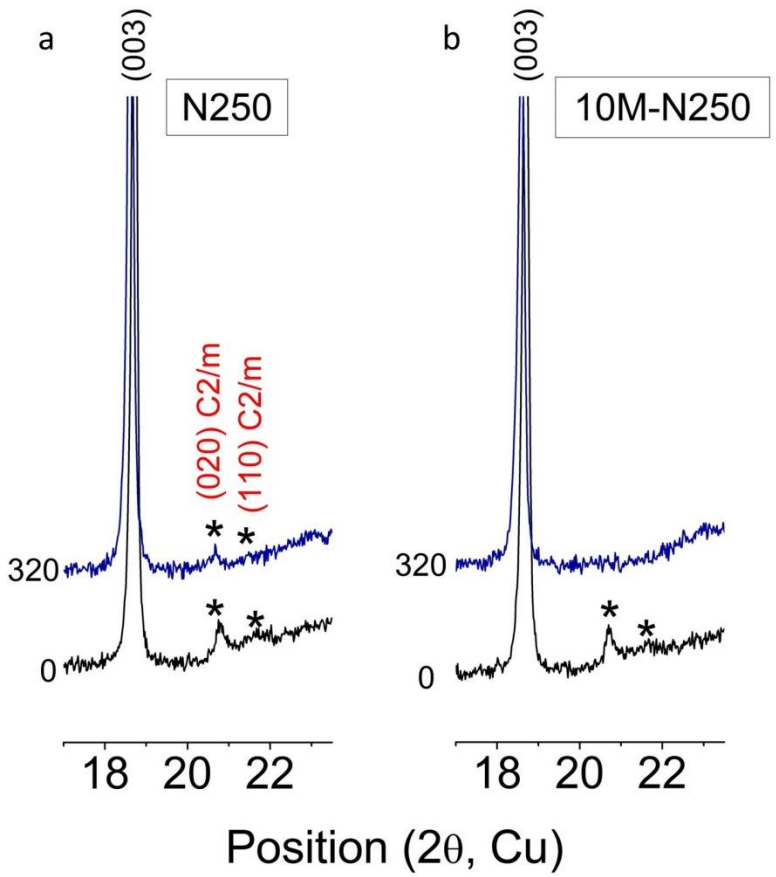

Figure S9. The XRD results that support the shortened electrochemical rejuvenation period after the thermal pre-rejuvenation. The XRD patterns of (a) N250 and (b) 10M-N250 electrodes before cycling (black) and after the 1st cycle at 20 mA/g (blue). For both electrodes, the first charge capacity was set to 320 mAh/g. While the in-plane ordering peaks (asterisks) from the C2/m Li_2MnO_3-like domain are visible for N250 after the first cycle, they are not seen for the 10M-N250. This result shows that a high-temperature pre-rejuvenation treatment accelerates the full rejuvenation (disruption of the C2/m medium-range order) of the Li-rich layered material upon cycling.

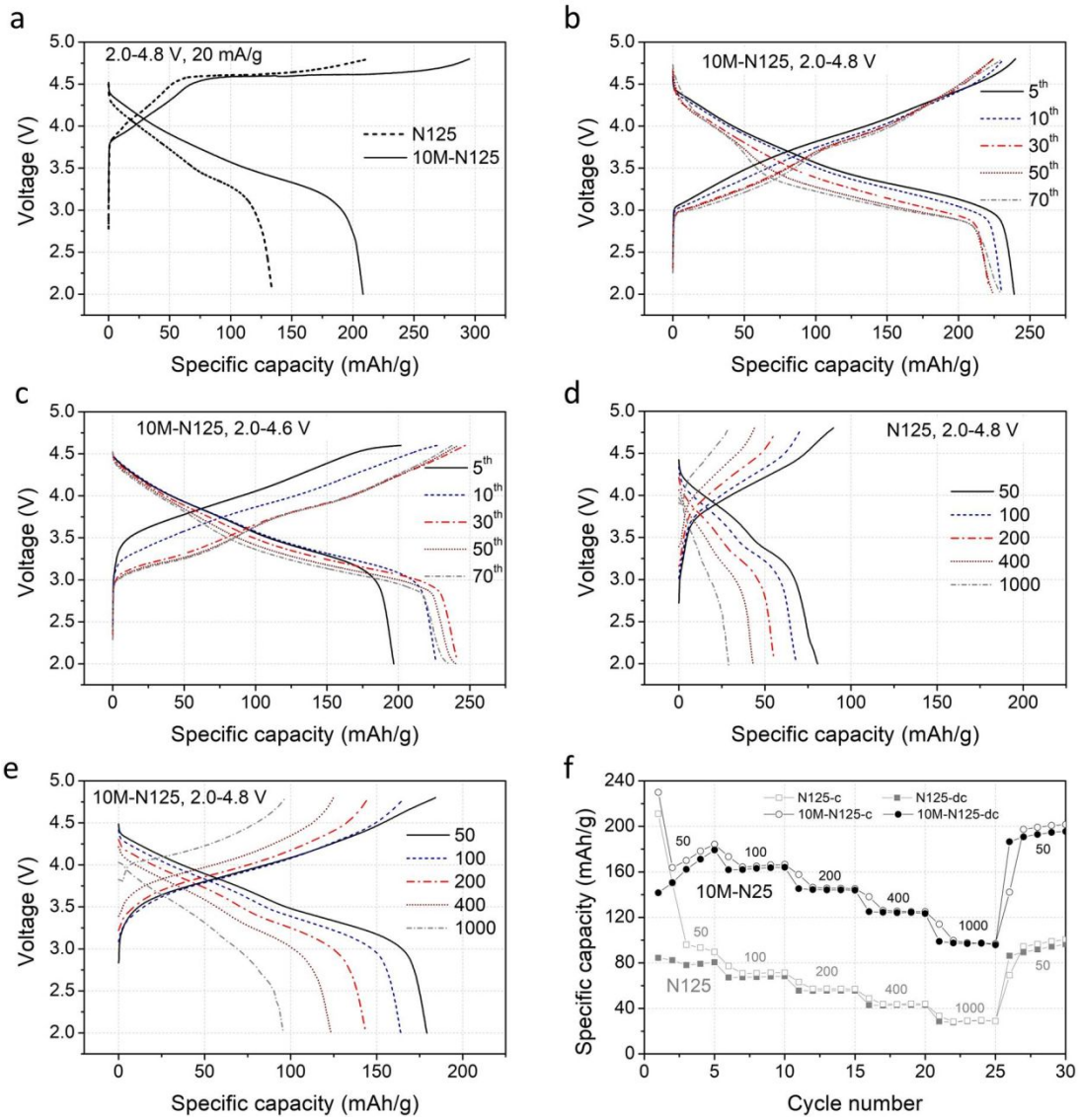

Figure S10. The thermal pre-rejuvenation effect on N125. (a) The first-cycle voltage profiles of N125 and 10M-N125 cathodes when they were cycled between 2.0 V and 4.8 V at 20 mA/g and room temperature. The extended cycle voltage profiles of 10M-N125 when it is cycled between (b) 2.0 V and 4.8 V, and (c) 2.0 V and 4.6 V at 20 mA/g. The representative voltage-profiles of the (d) N125 and (e) 10M-N125 when they are cycled at different rates (50, 100, 200, 400, 1000 mA/g). In this rate-test, N125 did not go through the activation cycle. (f) The charging and discharging capacity of the two samples during the rate-capability test. From these results, we can see that the 10M-N125 deliver substantially improved cycling performance compared to N125.

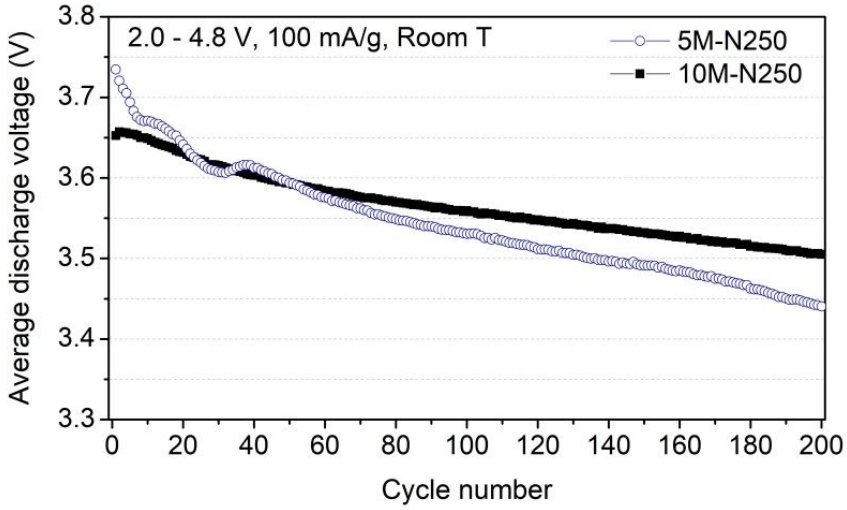

Figure S11. The average discharge voltage of 5M-N250 and 10M-N250 when they are cycled between 2.0 V and 4.8 V at 100 mA/g and room temperature.

Supplementary References

[1] M. C. Biesinger, B. P. Payne, A. P. Grosvenor, L. W. M. Lau, A. R. Gerson, R. St. C. Smart, Appl. Surf. Sci. 257 (2011) 2717–2730.

[2] Zhu, Z. Zhu, D. Yu, Y. Yang, C. Su, Y. Huang, Y. Dong, I. Waluyo, B. Wang, A. Hunt, X. Yao, J. Lee, W. Xue, J. Li, Nat. Energy, 4 (2019) 1049–1058.